

DEPARTMENT OF PHYSICS, UNIVERSITY OF JYVÄSKYLÄ

**JET TRANSVERSE MOMENTUM DISTRIBUTIONS
MEASURED BY ALICE**

**BY
TOMAS SNELLMAN**

PHD thesis

Supervisors: Jan Rak, Dong Jo Kim

Jyväskylä, Finland
December, 2018

3 Contents

4	1	Introduction	7
5	1.1	Quantum chromodynamics	8
6	1.1.1	Foundation of QCD	8
7	1.1.2	Asymptotic Freedom	9
8	1.2	Heavy ion physics	13
9	1.2.1	History	13
10	2	Features of Heavy-Ion Collisions	15
11	2.1	Collision Geometry	15
12	2.1.1	Nuclear Geometry	16
13	2.2	Hydrodynamical Modelling	19
14	2.3	Flow	22
15	2.3.1	Anisotropic Flow	23
16	2.3.2	High p_T Phenomena	24
17	2.4	Hard processes	29
18	2.4.1	Jet fragmentation	29
19	2.4.2	Jet hadronisation	29
20	2.4.3	Jet energy loss	30
21	2.4.4	Monte Carlo Implementations	34
22	2.5	QGP in Small systems	34
23	2.5.1	Collective phenomena	35
24	2.5.2	Absence of jet quenching	37
25	3	Experimental setup and data samples	39
26	4	Experimental Details	40
27	4.1	CERN	40
28	4.2	Large Hadron Collider	42
29	4.2.1	LHC experiments	43
30	4.3	ALICE	43
31	4.3.1	Tracking	44
32	4.3.2	TPC	45
33	4.3.3	TPC upgrade	45
34	4.3.4	Particle identification	45
35	4.3.5	Calorimeters	46

36	4.3.6	Forward detectors	46
37	4.3.7	Muon spectrometer	46
38	4.3.8	Trigger	46
39	5	Event and track selection	47
40	6	Analysis method	47
41	6.1	Jet Finding	47
42	6.1.1	Anti k_T algorithm	47
43	6.2	j_T	48
44	6.2.1	1 over j_T	48
45	6.3	Unfolding	49
46	6.3.1	Bayesian unfolding	50
47	6.3.2	Toy Monte Carlo	50
48	6.3.3	Pythia Response matrices	51
49	6.3.4	2D response matrices	52
50	6.3.5	Unfolding algorithm	52
51	6.3.6	Effect of number of iterations	52
52	6.3.7	Effect of different prior	53
53	6.3.8	Effect of p_T truncation	53
54	6.3.9	Unfolding closure test	53
55	6.4	Background	55
56	6.4.1	Perpendicular cone background	56
57	6.4.2	Random background	56
58	6.4.3	Auto-correlations	59
59	6.5	Fitting	59
60	7	Systematic uncertainties	60
61	8	TPC Upgrade?	62
62	9	Systematic errors	63
63	9.1	Background subtraction	63
64	9.2	Unfolding	63
65	9.3	Tracking	63
66	9.4	Combining systematics	63
67	10	Results	66
68	10.1	statistics	66
69	10.2	Data	66
70	10.3	Background	66
71	10.4	Inclusive results	68

72	10.5 Comparison between A and C side	68
73	10.6 Subtracted signal	68
74	10.7 Fitting	68
75	10.7.1 Results	68
76	10.8 Comparison to dihadron results	68
77	10.9 Different R parameters	72
78	11 Discussion	75
79	11.1 Discussion	75
80	12 Summary	77

81 List of Figures

82	1 QCD phase diagram	11
83	2 η/s vs $(T - T_c)/T_c$	12
84	3 The definitions of the Reaction Plane and Participant Plane coordinate systems	15
85	4 Interaction between partons in central and peripheral collisions.	16
86	5 An illustration of the multiplicity distribution in ALICE measurement with centrality classes.	17
87	6 The results of one Glauber Monte Carlo simulation.	20
88	7 Schematic representation of a heavy-ion collision	21
89	8 Charged particle spectra	22
90	9 Illustration of flow in momentum space in central and peripheral collisions.	23
91	10 Elliptic flow, v_2 from $p_T = 1$ to 60 GeV/ c	26
92	11 Measurements of the nuclear modification factor R_{AA} in central heavy-ion collisions	28
93	12 A comparison between observed $R_{AA}(\Delta\phi, p_T)$ and R_{AA} using v_2 . .	29
94	13 Elliptic flow, v_2 from $p_T = 1$ to 60 GeV/ c	31
95	14 Measurements of the nuclear modification factor R_{AA} in central heavy-ion collisions	33
96	15 A comparison between observed $R_{AA}(\Delta\phi, p_T)$ and R_{AA} using v_2 . .	34
97	16 Calculations of the intial energy density in small collision systems at RHIC and the resulting hydrodynamic evolution.	35
98	17 Two-particle correlation results in PbPb, pPb, and pp collisions at the LHC [].	36
99	18 RpA in proton-lead collisions	37
100	19 CERN collider complex	41

108	20	Illustration of \vec{j}_T . The jet fragmentation transverse momentum, \vec{j}_T , is defined as the transverse momentum component of the track momentum, \vec{p}_{track} , with respect to the jet momentum, \vec{p}_{jet}	48
109			
110	21	Results from unfolding in Toy Monte Carlo	51
111			
112	22	Unfolding with different number of iterations	53
113			
114	23	Effect of changing minimum jet p_T used in unfolding from 5 to 10 GeV	54
115			
116	24	Effect of changing minimum jet p_T used in unfolding from 5 to 10 GeV	54
117			
118	26	j_T Response matrices in single jet p_T bins	56
119			
120	27	Pythia closure test results. Fake tracks include also tracks that do exist in the true dataset, but for one reason or another were not given j_T values. j_T is only calculated for tracks that are associated with jets	57
121			
122	29	j_T signal with random bacgkround subtraction fits in different jet p_T bins	63
123			
124	30	Differences between perpendicular cone and random background subtraction in the resulting RMS values.	64
125			
126	31	j_T signal with random bacgkround subtraction fits in different jet p_T bins	64
127			
128	32	Differences between Bayesian and SVD unfolding in the resulting RMS values	64
129			
130	33	j_T background with two different methods	67
131			
132	34	Inclusive j_T with background	67
133			
134	35	Comparison of inclusive j_T distributions between A and C side for minimum bias and EMCAL triggered data.	69
135			
136	36	j_T signal with background subtracted	70
137			
138	37	Comparison of the effect of background method on j_T signal.	70
139			
140	38	j_T signal fits in different jet p_T bins	71
141			
142	39	RMS values extracted from the fits for the gaussian (narrow) and inverse gamma (wide) components	71
143			
144	40	RMS values extracted from the fits for the gaussian (narrow) and inverse gamma (wide) components	72
145			
141	41	Jet j_T results are compared to results obtained in the dihadron analysis. This is done both in jet p_T and trigger p_T bins by converting between them.	72
142			
143	42	Pythia R parameters j_T	73
144			
145	43	Pythia R parameters RMS	74

¹⁴⁶	44	Comparison of results with dihadron j_T results. Dihadron trigger p_T bins are converted to jet p_T bins using observed mean $p_{T\text{jet}}$ values in $p_{T\text{trigger}}$ bins. Dihadron results are for $0.2 < x_{ } < 0.4$	75
¹⁴⁷			
¹⁴⁸	45	PYTHIA R parameters j_T	76
¹⁴⁹			
¹⁵⁰	46	Results of calculating j_T with respect to the jet axis or the leading hadron. The assumption is that because the leading hadron is an imperfect estimate of the jet axis, low j_T tracks should on average be shifted to higher j_T	76
¹⁵¹			
¹⁵²			
¹⁵³			

154 1 Introduction

155 At sufficiently high energies quarks and gluons are no longer bound to hadrons,
156 but they form a deconfined state known as Quark-Gluon plasma (QGP). The
157 main goal of heavy ion physics is the study of QGP and its properties. One of the
158 experimental observables that is sensitive to the properties of QGP is the azimuthal
159 distribution of particles in the plane perpendicular to the beam direction.

160 When nuclei collide at non-zero impact parameter (non-central collisions), their
161 overlap region is asymmetric. This initial spatial asymmetry is converted via multi-
162 ple collisions into an anisotropic momentum distribution of the produced particles.
163 For low momentum particles ($p_T \lesssim 3$ GeV/c), this anisotropy is understood to
164 result from hydrodynamically driven flow of the QGP [1–5].

165 One way to characterize this anisotropy is with coefficients from a Fourier se-
166 ries parametrization of the azimuthal angle distribution of emitted hadrons. The
167 second order coefficient, v_2 which is also known as elliptic flow, shows clear depen-
168 dence on centrality. The collision geometry is mainly responsible for the elliptic
169 flow. Higher harmonics don't depend that much on centrality. These higher har-
170 monics carry information about the fluctuations in collisions. The event-by-event
171 fluctuations have an increasing importance in measurements and it has been ob-
172 served that measurements of elliptic flow in central collisions and measurements
173 of higher order harmonics are consistent with the assumption that flow in these
174 cases is mainly due to fluctuations [6].

175 At LHC energies $\sqrt{s_{NN}} = 2.76\text{GeV}$ it has been observed that in general there
176 is little difference to flow at RHIC energies. The v_2 coefficient is about 20% greater
177 at LHC than at RHIC, depending on the centrality bin. The particle identified
178 v_2 for kaons and pions follows the same trend. However it was observed that for
179 proton v_2 the quark number scaling does not work [7]. So far there is no agreement
180 of why this scaling breaks down at LHC or why it works so well at RHIC energies.

181 **1.1 Quantum chromodynamics**

182 **1.1.1 Foundation of QCD**

183 There are four known basic interactions in the universe: gravity, electromagnetic,
184 weak and strong interactions. The standard model of particle physics includes
185 three of these excluding the gravitational interaction. The theory of strong inter-
186 actions is known as Quantum Chromodynamics (QCD).

187 The development of QCD began after the introduction of new powerful particle
188 accelerators that were capable of particle physics research in the 1950s. Before this
189 particles were mainly discovered from cosmic rays. Positrons, neutrons and muons
190 were discovered in the 1930s and charged pions were discovered in 1947 []. The
191 neutral pion was discovered in 1950 [8].

192 The Lawrence Berkeley National Laboratory started the Bevalac accelerator in
193 1954, Super Proton Synchrotron (SPS) in CERN began operating in 1959 and the
194 Alternating Gradient Synchrotron at Brookhaven started in 1960. With an energy
195 of 33GeV AGS was the most powerful accelerator of that time. By the beginning
196 of 1960s several new particles had been discovered. These include antiprotons,
197 antineutrons, Δ -particles and the six hyperons (Ξ^0 , Ξ^- , Σ^\pm , Σ^0 and Λ).

198 Facing this number of different particles started the search for symmetries. Al-
199 ready in 1932 Heisenberg [9] had proposed an isospin model to explain similarities
200 between the proton and the neutron. In 1962 Gell-Mann and Ne'eman presented
201 that particles sharing the same quantum numbers (spin, parity) could be organ-
202 ised using the symmetry of SU(3). [10] Heisenberg's Isospin model followed the
203 symmetry of SU(2). Using the SU(3) model known baryons and mesons could be
204 presented as octets. This also lead to the discovery of the Ω^- particle since this
205 was missing from the SU(3) decoupler that included heavier baryons.

206 The most simple representation of SU(3) was a triplet. Inside this triplet
207 particles would have electric charges $2/3$ or $-1/3$. These had not been however
208 detected. In 1964 Gell-Mann [11] and Zweig proposed that baryons and mesons
209 would bound states of these three hypothetical triplet particles that Gell-Mann
210 called quarks. Now we know that these are the u , d and s quarks. This original
211 quark model was violating the Pauli exclusion principle. For example the Ω^-
212 particle is comprised of three s quarks which would have exactly the same quantum
213 states.

214 The first one to present the idea of colour was Greenberg already in 1964 [12].
215 In 1971 Gell-Mann and Frtizsch presented their model, which solved the antisym-
216 metry problem. They added a colour quantum number to quarks, which separated
217 quarks of the same species. In the new colour model the baryonic wave function
218 became

$$(qqq) \rightarrow (q_r q_g q_b - q_g q_r q_b + q_b q_r q_g - q_r q_b q_g + q_g q_b q_r - q_b q_g q_r), \quad (1)$$

219 The colour model was also supported by experimental evidence. The decay
220 rate of a neutral pion with the addition of colours is

$$\Lambda(\pi^0 \rightarrow \gamma\gamma) = \frac{\alpha^2}{2\pi} \frac{N_c^2}{3^2} \frac{m_\pi^3}{f_\pi^2}. \quad (2)$$

221 For $N_c = 3$ this gives 7.75eV and the measured value is (7.86 ± 0.54) eV [13].

222 Another observable that combines the colour information also to the number
223 of quark flavours is The Drell-Ratio R [14]

$$R = \frac{\sigma(e^+ + e^- \rightarrow \text{hadrons})}{\sigma(e^+ + e^- \rightarrow \mu^+ + \mu^-)} = N_c \sum_f Q_f^2. \quad (3)$$

224 This ratio has the numerical value 2 when including the three light quarks u , d
225 and s . When the collision energy reaches the threshold of heavy quark (c and
226 b) production processes this increases to $^{10}/3$ (for $f = u, d, s, c$) and $^{11}/3$ (for $f =$
227 u, d, s, c, b). The threshold of $t\bar{t}$ production, $\sqrt{s} \approx 350$ GeV has not been reached
228 so far by any e^+e^- colliders.

229 The colour model explained why no free quarks had been observed. Only colour
230 neutral states are possible. The simplest ways of producing a colour neutral object
231 are the combination of three quarks, and the combination of a quark-antiquark
232 pair. These are known as baryons and mesons.

233 After the addition of colour the main ingredients of QCD had been established.
234 The final quantum field theory of Quantum Chromodynamics formed quickly be-
235 tween 1972 and 1974. Main part of this was the work Gross, Wilczek, Politzer
236 and George did for non-abelian gauge field theories [15–19]. Gross, Wilczek and
237 Politzer received the Nobel Prize in Physics for their work. The role of gluons was
238 as a colour octet was presented by Fritzsch, Gell-Mann and Leutwyler in 1973 [20].
239 The theory had now 8 massless gluons to mediate the strong interaction.

240 However, these gluons had not been discovered. Indirect evidence of the ex-
241 istence had been seen as it was observed that only about half of the momentum
242 of protons was transported by the quarks [21]. Direct evidence should be seen in
243 electron-electron collisions as a third, gluonic, jet in addition to two quark jets.
244 Three jet events were first seen in 1979 at the PETRA accelerator at DESY [22–24].

245 1.1.2 Asymptotic Freedom

246 In Quantum Electrodynamics (QED) The electric charge is screened. In the
247 vicinity of a charge, the vacuum becomes polarized. Virtual charged particle-
248 antiparticle pairs around the charge are arranged so that opposing charges face

each other. Since the pairs also include an equal amount opposite charge compared to the original charge the average charge seen by an observer at a distance is smaller. When the distance to the charge increases the effective charge decreases until the coupling constant of QED reaches the fine-structure constant $\alpha = \frac{1}{137}$.

Contrary to QED QCD is a non-abelian theory. In other words the generators of the symmetry group of QCD, SU(3), do not commute. This has the practical consequence that gluons interact also with other gluons, whereas in QED the neutral carrier particles, photons, only interact with charged particles. There is screening also in QCD because of the colour charges, but in addition to that there is antiscreening because of the gluon interactions. In QCD the antiscreening effect is stronger than screening. For larger distances to the colour charge the coupling constant is larger. This explains why no free colour charges can be observed. When the distance between charges increases the interaction strengthens until it is strong enough to produce a new quark-antiquark pair.

On the other hand, at very small distances the coupling constant approaches 0. This is called asymptotic freedom. For large energies and small distances the coupling constant is negligible. In 1975 Collins [25] predicted a state where individual quarks and gluons are no longer confined into bound hadronic states. Instead they form a bulk QCD matter that Edward Shuryak called Quark-Gluon plasma in his 1980 review of QCD and the theory of superdense matter [26]. QGP can be seen as a separate state of matter. A schematic view of a phase diagram for QCD matter is shown in Fig. 1.

In the early universe at the age of 10^{-6} s after the Big Bang the conditions preferred the existence of QGP instead of hadronic matter. Nowadays bulk QCD matter, its properties and its phase transitions between hadronic matter and the quark-gluon plasma (QGP) can be explored in the laboratory, through collisions of heavy atomic nuclei at ultra-relativistic energies. The study of QCD matter at high temperature is of fundamental and broad interest. The phase transition in QCD is the only phase transition in a quantum field theory that can be probed by any present or foreseeable technology.

One important property of the QGP is the shear viscosity to entropy ratio, η/s . It is believed that this ratio has an universal minimum value of $1/4\pi \approx 0.8$, which holds for all substances. This limit would be reached in the strong coupling limit of certain gauge theories [28]. The temperature dependance of the ratio is shown in Fig. 2. The minimum value of η/s is found in the vicinity of the critical temperature, T_c [29]. Finding the η/s values in QGP matter would therefore also provide a way of determining the critical point of QCD matter.

The η/s value for the matter created in Au-Au collisions at RHIC ($\sqrt{s_{NN}}$) has been estimated to be 0.09 ± 0.015 [29], which is very close to the lowest value for a wide class of thermal quantum field theories [28] for all relativistic quantum field

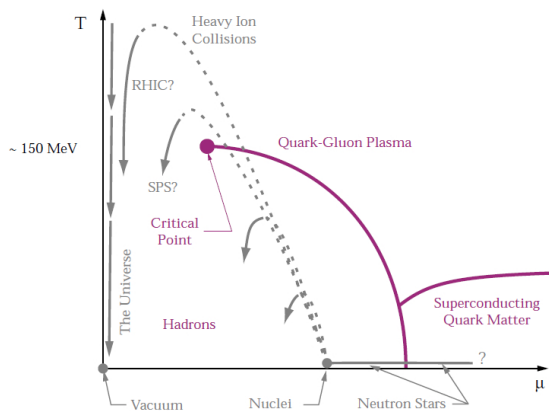


Figure 1: A schematic outline for the phase diagram of QCD matter at ultra-high density and temperature. The quark chemical potential μ that is on the x-axis represents the imbalance between quarks and antiquarks. At zero temperature this corresponds to the number of quarks but at higher temperatures there are also additional pairs of quarks and antiquarks. Along the horizontal axis the temperature is zero, and the density is zero up to the onset transition where it jumps to nuclear density, and then rises with increasing μ . Neutron stars are in this region of the phase diagram, although it is not known whether their cores are dense enough to reach the quark matter phase. Along the vertical axis the temperature rises, taking us through the crossover from a hadronic gas to the quark-gluon plasma. This is the regime explored by high-energy heavy-ion colliders. [27]

289 theories at finite temperature and zero chemical potential. This suggests that the
 290 the matter created goes through a phase where it is close to the critical point of
 291 QCD.

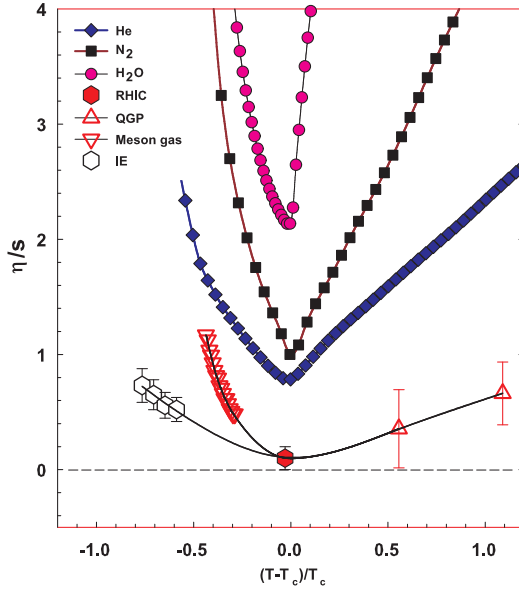


Figure 2: η/s as a function of $(T - T_c)/T_c$ for several substances as indicated. The calculated values for the meson-gas have an associated error of $\sim 50\%$. The lattice QCD value $T_c = 170$ MeV is assumed for nuclear matter. The lines are drawn to guide the eye. [29]

292 **1.2 Heavy ion physics**

293 The Quark Gluon Plasma (QGP) is experimentally accessible by colliding heavy
294 ions at high energies. Nowadays research of Heavy-Collisions is mainly performed
295 at two particle colliders; the The Relativistic Heavy Ion Collider (RHIC) at BNL
296 in New York, USA and he Large Hadron Collider (LHC) at CERN in Switzer-
297 land. Energy densities at these colliders should be enough to produce QGP and
298 convincing evidence of the creation has been seen at both colliders.

299 The development of heavy ion physics is strongly connected to the development
300 of particle colliders. Experimental study of relativistic heavy ion collisions has been
301 carried out for three decades, beginning with the Bevalac at Lawrence Berkeley
302 National Laboratory (LBNL) [30], and continuing with the AGS at Brookhaven
303 National Laboratory (BNL) [31], CERN SPS [32], RHIC at BNL and LHC at
304 CERN. The first colliders could not produce enough energy to create QGP matter
305 so they could only probe the hadronic state.

306 The collective motion of matter in a heavy-ion collision has been modeled using
307 several models e.g. the Blast wave Model [33] has been used successfully. Another
308 model growing in popularity is the hydrodynamical approach which is further
309 discussed in section 2.2.

310 **1.2.1 History**

311 The first heavy-ion collisions were done at the Bevalac experiment at the Lawrence
312 Berkeley National Laboratory [30] and at the Joint Institute for Nuclear Research
313 in Dubna [34] at energies up to 1GeV per nucleon. In 1986 the Super Proton
314 Synchrotron (SPS) at CERN started to look for QGP signatures in O+Pb col-
315 lisions. The center-of-mass energy per colliding nucleon pair ($\sqrt{s_{NN}}$) was 19.4
316 GeV [32]. These experiments did not find any decisive evidence of the existence
317 of QGP. In 1994 a heavier lead (Pb) beam was introduced for new experiments
318 at $\sqrt{s_{NN}} \approx 17$ GeV. At the same time the Alternating Gradient Synchrotron
319 (AGS) at BNL, Brookhaven collided ions up to ^{32}S with a fixed target at energies
320 up to 28GeV [31]. Although the discovery of a new state of matter was reported
321 at CERN, these experiments provided no conclusive evidence of QGP. Now SPS
322 is used with 400 GeV proton beams for fixed-target experiments, such as the SPS
323 Heavy Ion and Neutrino Experiment (SHINE) [35], which tries to search for the
324 critical point of strongly interacting matter.

325 The Relativistic Heavy Ion Collider (RHIC) at BNL in New York, USA started
326 its operation in 2000. The top center-of-mass energy per nucleon pair at RHIC, 200
327 GeV, was reached in the following years. The results from the experiments at RHIC
328 have provided a lot of convincing evidences that QGP was created [1,2,36,37]. The
329 newest addition to the group of accelerators capable of heavy-ion physics is the

³³⁰ Large Hadron Collider (LHC) at CERN, Switzerland. LHC started operating in
³³¹ November 2009 with proton-proton collisions. First Pb-Pb heavy ion runs started
³³² in November 2010 with $\sqrt{s_{NN}} = 2.76$ TeV, over ten times higher than at RHIC.
³³³ Among the six experiments at LHC, the Large Ion Collider Experiment (ALICE)
³³⁴ is dedicated to heavy ion physics. Also CMS and ATLAS have active heavy ion
³³⁵ programs.

336 2 Features of Heavy-Ion Collisions

337 2.1 Collision Geometry

338 In contrast to protons atomic nuclei are objects with considerable transverse size.
 339 The properties of a heavy-ion collision depend strongly on the impact parameter
 340 b which is the vector connecting the centers of the two colliding nuclei at their
 341 closest approach. One illustration of a heavy-ion collision is shown in Fig. 3.

342 Impact parameter defines the reaction plane which is the plane spanned by b
 343 and the beam direction. Ψ_{RP} gives the angle between the reaction plane and some
 344 reference frame angle. Experimentally the reference frame is fixed by the detector
 345 setup. Reaction plane angle cannot be directly measured in high energy nuclear
 collisions, but it can be estimated with the event plane method [38].

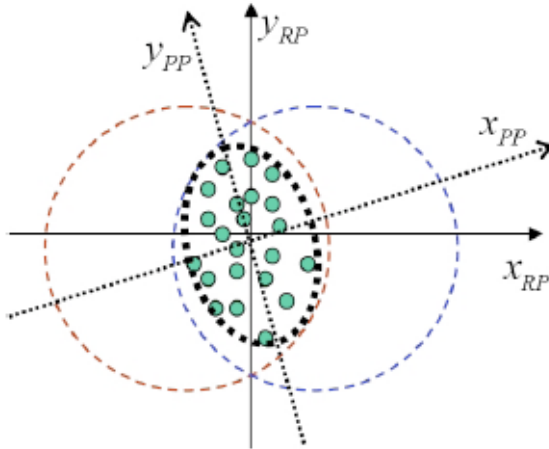


Figure 3: The definitions of the Reaction Plane and Participant Plane coordinate systems [39]. The dashed circles represent the two colliding nuclei and the green dots are partons that take part in the collision. x_{PP} and x_{RP} are the participant and reaction planes. The angle between x_{RP} and x_{PP} is given by Eq. (4). y_{PP} and y_{RP} are lines perpendicular to the participant and reaction planes.

346
 347 Participant zone is the area containing the participants. The distribution of
 348 nucleons in the nucleus exhibits time-dependent fluctuations. Because the nucleon
 349 distribution at the time of the collision defines the participant zone, the axis of
 350 the participant zone fluctuates and can deviate from the reaction plane. The angle
 351 between the participant plane and the reaction plane is defined by [40]

$$\psi_{PP} = \arctan \frac{-2\sigma_{xy}}{\sigma_y^2 - \sigma_x^2 + \sqrt{(\sigma_y^2 - \sigma_x^2)^2 + 4\sigma_{xy}^2}}, \quad (4)$$

352 where the σ -terms are averaged over the energy density.

$$\sigma_y^2 = \langle y^2 \rangle - \langle y \rangle^2, \sigma_x^2 = \langle x^2 \rangle - \langle x \rangle^2, \sigma_{xy} = \langle xy \rangle - \langle x \rangle \langle y \rangle \quad (5)$$

353 The impact parameter is one way to quantize the centrality of a heavy-ion
 354 collision but it is impossible to measure in a collision. It can be estimated from
 355 observed data using theoretical models, but this is always model-dependent and
 356 to compare results from different experiments one needs an universal definition for
 357 centrality. The difference between central and peripheral collisions is illustrated
 358 in Fig. 4. In a central collision the overlap region is larger than in a peripheral
 359 collision. Larger overlap region translates into a larger number of nucleons partici-
 360 pating in the collision, which in turn leads to a larger number of particles produced
 361 in the event.

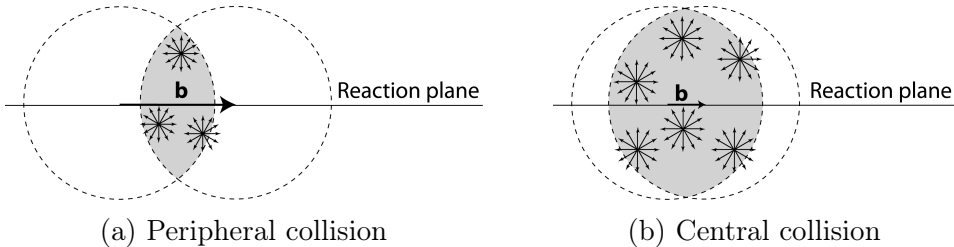


Figure 4: Interaction between partons in central and peripheral collisions. The snowflakes represent elementary parton-parton collisions. When the impact parameter b is large the number of elementary collisions is small. Particle production is small. Smaller impact parameter increases the number of elementary collisions. This increases particle production.

362 Usually centrality is defined by dividing collision events into percentile bins by
 363 the number participants or experimentally by the observed multiplicity. Centrality
 364 bin 0-5% corresponds to the most central collisions with the highest multiplicity
 365 and higher centrality percentages correspond to more peripheral collisions with
 366 lower multiplicities. A multiplicity distribution from ALICE measurements [41]
 367 illustrating the centrality division is shown in Fig. 5. The distribution is fitted
 368 using a phenomenological approach based on a Glauber Monte Carlo [42] plus a
 369 convolution of a model for the particle production and a negative binomial distri-
 370 bution.

371 2.1.1 Nuclear Geometry

372 To model heavy-ion collisions one must first have a description as good as possible
 373 of the colliding objects. Atomic nuclei are complex ensembles of nucleons. The
 374 nuclei used in heavy-ion physics have in the order of 200 nucleons. Mostly used

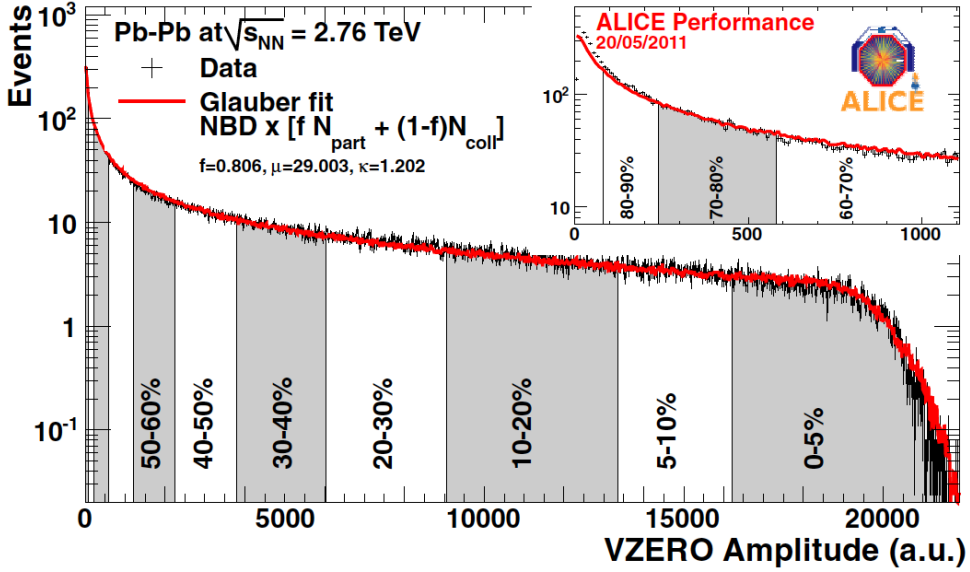


Figure 5: An illustration of the multiplicity distribution in ALICE measurements. The red line shows the fit of the Glauber calculation to the measurement. The data is divided into centrality bins [41]. The size of the bins corresponds to the indicated percentile.

375 nuclei are ^{208}Pb at LHC and ^{197}Au at RHIC. The distribution of these nucleons
 376 within a nucleus is not uniform and is subject to fluctuations in time.

377 Nuclear geometry in heavy-ion collisions is often modelled with the Glauber
 378 Model. The model was originally developed to address the problem of high energy
 379 scattering with composite particles. Glauber presented his first collection of papers
 380 and unpublished work in his 1958 lectures [43]. In the 1970's Glauber's work
 381 started to have utility in describing total cross sections. Maximon and Czyz applied
 382 it to proton-nucleus and nucleus-nucleus collisions in 1969 [44].

383 In 1976 [45] Białas, Bleszyński, and Czyz applied Glauber's approach to
 384 inelastic nuclear collisions. Their approach introduced the basic functions used in
 385 modern language including the thickness function and the nuclear overlap function.
 386 Thickness function is the integral of the nuclear density over a line going through
 387 the nucleus with minimum distance s from its center

$$T_A(s) = \int_{-\infty}^{\infty} dz \rho(\sqrt{s^2 + z^2}). \quad (6)$$

388 This function gives the thickness of the nucleus, i.e. the amount material seen by
 389 a particle passing through it.

³⁹⁰ Overlap function is an integral of the thickness functions of two colliding nuclei
³⁹¹ over the overlap area. This can be seen as the material that takes part in the
³⁹² collision. It is given as a function of the impact parameter b

$$T_{AB}(b) = \int ds^2 T_A(\bar{s}) T_B(\bar{s} - \bar{b}) \quad (7)$$

³⁹³ The average overlap function, $\langle T_{AA} \rangle$, in an A-A collisions is given by [46]

$$\langle T_{AA} \rangle = \frac{\int T_{AA}(b) db}{\int (1 - e^{-\sigma_{pp}^{inel} T_{AA}(b)}) db}. \quad (8)$$

³⁹⁴ Using $\langle T_{AA} \rangle$ one can calculate the mean number of binary collisions

$$\langle N_{coll} \rangle = \sigma_{pp}^{inel} \langle T_{AA} \rangle, \quad (9)$$

³⁹⁵ where the total inelastic cross-section, σ_{pp}^{inel} , gives the probability of two nucleons
³⁹⁶ interacting. The number of binary collisions is related to the hard processes in a
³⁹⁷ heavy-ion collision. Each binary collision has equal probability for direct produc-
³⁹⁸ tion of high-momentum partons. Thus the number of high momentum particles is
³⁹⁹ proportional to $\langle N_{coll} \rangle$.

⁴⁰⁰ Soft production on the other hand is related to the number of participants.
⁴⁰¹ It is assumed that in the binary interactions participants get excited and further
⁴⁰² interactions are not affected by previous interactions because the time scales are
⁴⁰³ too short for any reaction to happen in the nucleons. After the interactions ex-
⁴⁰⁴ cited nucleons are transformed into soft particle production. Production does not
⁴⁰⁵ depend on the number of interactions a nucleon has gone through. The average
⁴⁰⁶ number of participants, $\langle N_{part} \rangle$ can also be calculated from the Glauber model

$$\begin{aligned} \langle N_{part}^{AB}(b) \rangle &= \int ds^2 T_A(\bar{s}) \left[1 - \left[1 - \sigma_{NN} \frac{T_B(\bar{s} - \bar{b})}{B} \right]^B \right] \\ &+ \int ds^2 T_B(\bar{s}) \left[1 - \left[1 - \sigma_{NN} \frac{T_A(\bar{s} - \bar{b})}{A} \right]^A \right]. \end{aligned} \quad (10)$$

⁴⁰⁷ Glauber calculations require some knowledge of the properties of the nuclei.
⁴⁰⁸ One requirement is the nucleon density distribution, which can be experimen-
⁴⁰⁹ tally determined by studying the nuclear charge distribution in low-energy elec-
⁴¹⁰ tron scattering experiments [42]. The nucleon density is usually parametrized by
⁴¹¹ a Woods-Saxon distribution

$$\rho(r) = \frac{\rho_0}{1 + \exp\left(\frac{r-R}{a}\right)}, \quad (11)$$

412 where ρ_0 is the nucleon density in center of the nucleus, R is the nuclear radius
 413 and a parametrizes the depth of the skin. The density stays relatively constant as
 414 a function of r until around R where it drops to almost 0 within a distance given
 415 by a .

416 Another observable required in the calculations is the total inelastic nucleon-
 417 nucleon cross-section $\sigma_{\text{inel}}^{\text{NN}}$. This can be measured in proton-proton collisions at
 418 different energies.

419 There are two often used approaches to Glauber calculations. The optical ap-
 420 proximation is one way to get simple analytical expressions for the nucleus-nucleus
 421 interaction cross-section, the number of interacting nucleons and the number of
 422 nucleon-nucleon collisions. In the optical Glauber it is assumed that during the
 423 crossing of the nuclei the nucleons move independently and they will be essentially
 424 undeflected.

425 With the increase of computational power at hand the Glauber Monte Carlo
 426 (GMC) approach has emerged as a method to get a more realistic description of
 427 the collisions. In GMC the nucleons are distributed randomly in three-dimensional
 428 coordinate system according to the nuclear density distributions. Also nuclear
 429 parameters, like the radius R can be sampled from a distribution. A heavy-ion
 430 collision is then treated as a series of independent nucleon-nucleon collisions, where
 431 in the simplest model nucleons interact if their distance in the plane orthogonal
 432 to the beam axis, d , satisfies

$$d < \sqrt{\sigma_{\text{inel}}^{\text{NN}}} \quad (12)$$

433 The average number of participants and binary collisions can then be determined
 434 by simulating many nucleus-nucleus collisions. The results of one GMC Pb-Pb
 435 event with impact parameter $b = 9.8\text{fm}$ is shown in Fig. 6

436 2.2 Hydrodynamical Modelling

437 The relativistic version of hydrodynamics has been used to model the deconfined
 438 phase of a heavy-ion collision with success. Heavy-ion collisions produce many
 439 hadrons going into all directions. It is expected that tools from statistical physics
 440 would be applicable to this complexity [47]. The power of relativistic hydrodyn-
 441 amics lies in its simplicity and generality. Hydrodynamics only requires that there is
 442 local thermal equilibrium in the system. In order to reach thermal equilibrium the
 443 system must be strongly coupled so that the mean free path is shorter than the
 444 length scales of interest [48].

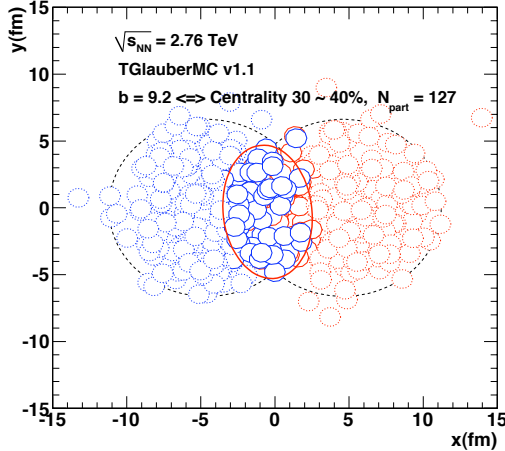


Figure 6: The results of one Glauber Monte Carlo simulation. Big circles with black dotted boundaries represent the two colliding nuclei. The participant zone is highlighted with the solid red line. Small red and blue circles represent nucleons. Circles with thick boundaries are participants i.e. they interact with at least one nucleon from the other nucleus. Small circles with dotted boundaries are spectators which do not take part in the collision.

445 The use of relativistic hydrodynamics in high-energy physics dates back to
 446 Landau [49] and the 1950's, before QCD was discovered. Back then it was used
 447 in proton-proton collisions. Development of hydrodynamics for the use of heavy-
 448 ion physics has been active since the 1980's, including Bjorken's study of boost-
 449 invariant longitudinal expansion and infinite transverse flow [?]. Major steps were
 450 taken later with the inclusion of finite size and and dynamically generated trans-
 451 verse size [?, ?], a part of which was done at the University of Jyväskylä. The role
 452 of hydrodynamics in heavy-ion physics was strengthened when QGP was observed
 453 to behave like a liquid by RHIC [1].

454 The evolution of a heavy-ion event can be divided into four stages. A schematic
 455 representation of the evolution of the collisions is shown in Fig. 7. Stage 1 follows
 456 immediately the collision. This is known as the pre-equilibrium stage. Hydrody-
 457 namic description is not applicable to this regime because thermal equilibrium is
 458 not yet reached. The length of this stage is not known but it is assumed to last
 459 about $1 \text{ fm}/c$ in proper time τ .

460 The second stage is the regime where thermal equilibrium or at least near-
 461 equilibrium is reached. In this stage hydrodynamics should be applicable if the
 462 temperature is above the deconfinement temperature [48]. This lasts about $5 - 10 \text{ fm}/c$ until the temperature of the system sinks low enough for hadronization to

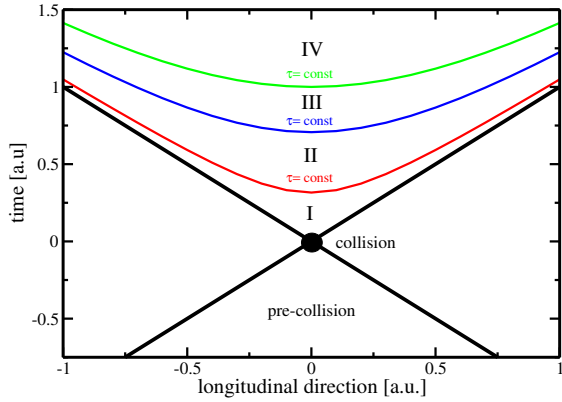


Figure 7: Schematic representation [48] of a heavy-ion collision as the function of time and longitudinal coordinates z . The various stages of the evolution correspond to proper time $\tau = \sqrt{t^2 - z^2}$ which is shown as hyperbolic curves separating the different stages.

464 occur. Now the system loses its deconfined, strongly coupled, state and hydrodynamics
 465 can no longer be used. The third stage is the hadron gas stage where the
 466 hadrons still interact. This ends when hadron scattering becomes rare and they
 467 no longer interact. In the final stage hadrons are free streaming and they fly in
 468 straight lines until they reach the detector.

469 The hydrodynamical approach treats the ensemble of particles as a fluid. It
 470 uses basic equations from hydrodynamics and thermodynamics but with a few
 471 modifications to account for the relativistic energies. The calculation is based
 472 on a collection of differential equations connecting the local thermal variables like
 473 temperature, pressure etc. to local velocities of the fluid. One also needs equations
 474 of state that connect the properties of the matter, e.g. temperature and pressure
 475 to density. Given initial conditions and equations of state the calculation gives the
 476 time-evolution of the system.

477 At first only ideal hydrodynamics was used. Ideal hydrodynamics does not
 478 include viscosity but it is a relatively good approximation and it could predict
 479 phenomena like elliptic flow. For more detailed calculations also viscosity must be
 480 considered and viscosity itself is an interesting property of QGP.

481 In this thesis I compare my results of identified particle flow to calculations from
 482 two hydrodynamical models; VISHNU model by Song *et al.* [50] and calculations
 483 by Niemi *et al.* [51].

484 2.3 Flow

485 In a heavy-ion collision the bulk particle production is known as flow. The pro-
 486 duction is mainly isotropic but a lot of studies including my thesis focus on the
 487 small anisotropies. After the formation of the QGP, the matter begins to expand
 488 as it is driven outwards by the strong pressure difference between the center of the
 489 collision zone and the vacuum outside the collision volume. The pressure-driven
 490 expansion is transformed into flow of low-momentum particles in the hadroniza-
 491 tion phase. Since the expansion is mainly isotropic the resulting particle flow is
 492 isotropic with small anisotropic corrections that are of the order of 10% at most.
 493 The isotropic part of flow is referred to as radial flow.

494 The transverse momentum spectra dN/dp_T in heavy-ion collisions is shown

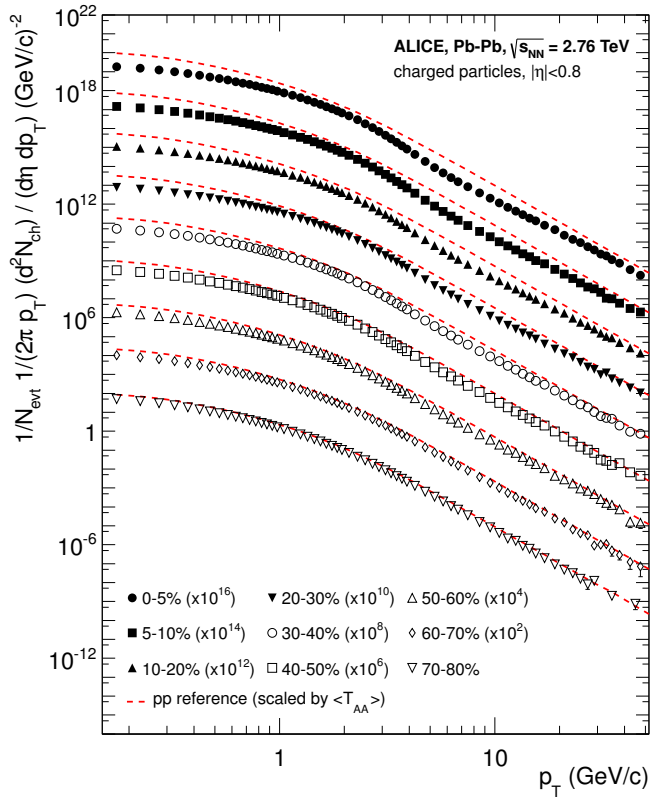


Figure 8: Charged particle spectra measured by ALICE [52] for the 9 centrality classes given in the legend. The distributions are offset by arbitrary factors given in the legend for clarity. The distributions are offset by arbitrary factors given in the legend for clarity. The dashed lines show the proton-proton reference spectra scaled by the nuclear overlap function determined for each centrality class and by the Pb-Pb spectra scaling factors [52].

495 in Fig. 8. The vast majority of produced particles have small p_T . The difference
 496 between the yield of 1 GeV/c and 4 GeV/c particles is already 2-3 orders of mag-
 497 nitude. Any observables that are integrated over p_T are therefore dominated by
 498 the small momentum particles.

499 2.3.1 Anisotropic Flow

500 In a non-central heavy-ion collision the shape of the impact zone is almond-like.
 501 In peripheral collisions the impact parameter is large which means a strongly
 502 asymmetric overlap region. In a central collision the overlap region is almost
 503 symmetric in the transverse plane. In this case the impact parameter is small.
 504 Collisions with different impact parameters are shown in Fig. 4.

505 The pressure gradient is largest in-plane, in the direction of the impact pa-
 506 rameter b , where the distance from high pressure, at the collision center, to low
 507 pressure, outside the overlap zone, is smallest. This leads to stronger collective
 508 flow into in-plane direction, which in turn results in enhanced thermal emission
 509 through a larger effective temperature into this direction, as compared to out-of-
 510 plane [3, 4, 53]. The resulting flow is illustrated in Fig. 9. Flow with two maxima
 511 in the direction of the reaction plane is called elliptic flow. This is the dominant

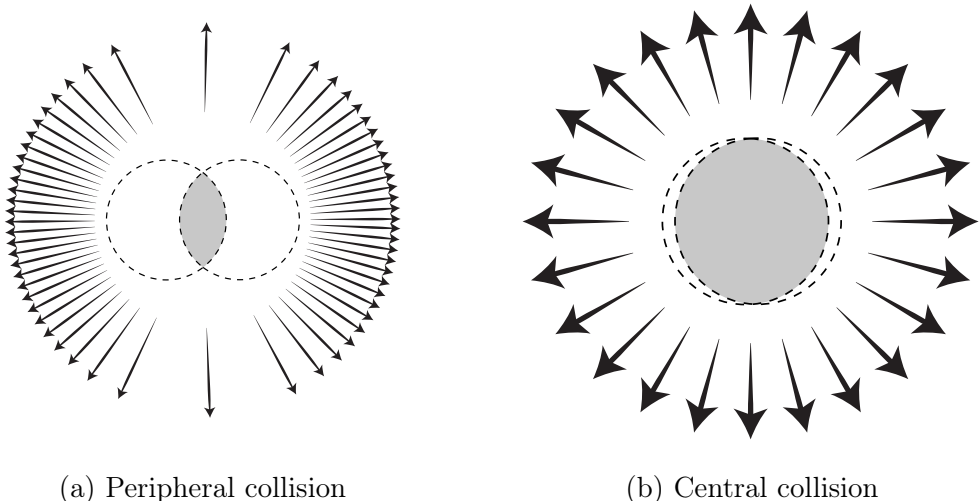


Figure 9: Illustration of flow in momentum space in central and peripheral collisions. The density of the arrows represent the magnitude of flow seen at a large distance from the collision in the corresponding azimuthal direction. In a peripheral collision momentum flow into in-plane direction is strong and flow into out-of-plane direction is weak. In a central collision anisotropy in flow is smaller, but the total yield of particles is larger.

512 part of anisotropic flow. Also more complex flow patterns can be identified. The
513 most notable of these is the triangular flow, which is mainly due to fluctuations in
514 the initial conditions.

515 Flow is nowadays usually quantified in the form of a Fourier composition

$$E \frac{d^3N}{dp^3} = \frac{1}{2\pi} \frac{d^2N}{p_T dp_T d\eta} \left(1 + \sum_{n=1}^{\infty} 2v_n(p_T, \eta) \cos(n(\phi - \Psi_n)) \right), \quad (13)$$

516 where the coefficients v_n give the relative strengths of different anisotropic flow
517 components and the overall normalisation gives the strength of radial flow. Elliptic
518 flow is represented by v_2 and v_3 represents triangular flow. The first coefficient,
519 v_1 , is connected to directed flow. This will however in total be zero because of
520 momentum conservation. It can be nonzero in some rapidity or momentum regions
521 but it must be canceled by other regions.

522 The first approaches to quantifying the anisotropy of flow did not use the
523 Fourier composition. Instead they approached the problem with a classic event
524 shape analysis using directivity [54] or sphericity [3, 55] to quantify the flow.

525 The first experimental studies of anisotropy were performed at the AGS [56]
526 in 1993. They noted that the anisotropy of particle production in one region
527 correlates with the reaction plane angle defined in another region.

528 The first ones to present the Fourier decomposition were Voloshin and Zhang in
529 1996 [57]. This new approach was useful for detecting different types of anisotropy
530 in flow, since the different Fourier coefficients give different harmonics in flow.
531 They also show the relative magnitude of each harmonic compared to radial flow.

532 Some parts of the Fourier composition approach were used for Au-Au collisions
533 at $\sqrt{s_{NN}} = 11.4\text{GeV}$ at AGS in 1994 [58]. This analysis still focused on event
534 shapes but they constructed these shapes using Fourier composition from different
535 rapidity windows.

536 2.3.2 High p_T Phenomena

537 The measurement of anisotropic flow coefficients can be extended to very high
538 transverse momenta p_T . High p_T measurements of v_2 from CMS [59] are shown
539 in Fig. 13. For high transverse momenta v_2 values are positive and they decrease
540 slowly as a function of p_T . At high transverse momentum the v_2 values don't,
541 however, represent flow.

542 High momentum particles are very rare and they are only produced in the
543 initial collisions. After they are created they escape the medium before a thermal
544 equilibrium is reached. Thus they are not part of the pressure-driven collective
545 expansion. Instead high momentum yield is suppressed because of energy loss in
546 the medium. When propagating through the medium these partons lose energy as

547 they pass through the medium. This is referred to as jet quenching. Jet quenching
548 depends on the path lengths through the medium. Thus anisotropy in this region
549 is mainly dependent on the collision geometry and density of medium.

550 The energy loss of partons in medium is mainly due to QCD bremsstrahlung
551 and to elastic scatterings between the parton and the medium.

552 In elastic scatterings the recoil energy of the scattered partons are absorbed
553 by the thermal medium, which reduces the energy of the initial parton. The mean
554 energy loss from elastic scatterings can be estimated by

$$\langle \Delta E \rangle_{el} = \sigma \rho L \langle E \rangle_{1scatt} \propto L, \quad (14)$$

555 where σ is the interaction cross section and $\langle E \rangle_{1scatt}$ is the mean energy transfer
556 of one individual scattering [60].

557 Another energy loss mechanism is medium-induced radiation. In QCD this
558 radiation is mainly due to the elementary splitting processes, $q \rightarrow qg_r$ and $g \rightarrow gg_r$.
559 Assuming that the parton is moving with the speed of light radiation energy loss
560 can be estimated by

$$\langle \Delta E \rangle_{rad} \propto T^3 L^2, \quad (15)$$

561 where L is the length of the medium and T is its temperature [61].

562 There are several models that attempt to describe the nature of the energy loss
563 mechanism. The most used models can be divided into four formalisms.

564 In the Gyulassy-Levai-Vitev (GLV) [62] opacity expansion model the radiative
565 energy loss is considered on a few scattering centers N_{scatt} . The radiated gluon
566 is constructed by pQCD calculation as summing up the relevant scattering am-
567 plitudes in terms of the number of scatterings. Another approach into opacity
568 expansion is the ASW model by Armesto, Salgado and Wiedermann [63].

569 Thermal effective theory formulation by Arnold, Moore and Yaffe (AMY) [64]
570 uses dynamical scattering centers. It is based on leading order pQCD hard thermal
571 loop effective field theory. This model assumes that because of the high temper-
572 ature of the plasma the strong coupling constant can be treated as small. The
573 parton propagating through the medium will lose energy from soft scatterings and
574 hard scatterings.

575 The above models calculate the energy loss while the parton propagates through
576 the medium, focusing on the pQCD part. The higher twist (HT) approach by Wang
577 and Guo [65] implements the energy loss mechanism in the energy scale evolution
578 of the fragmentation functions.

579 The last category is formed by the Monte Carlo methods. The PYTHIA event
580 generator [66] is widely used in high-energy particle physics. Two Monte Carlo
581 models based on PYTHIA describing the energy loss mechanism are PYQUEN [67]

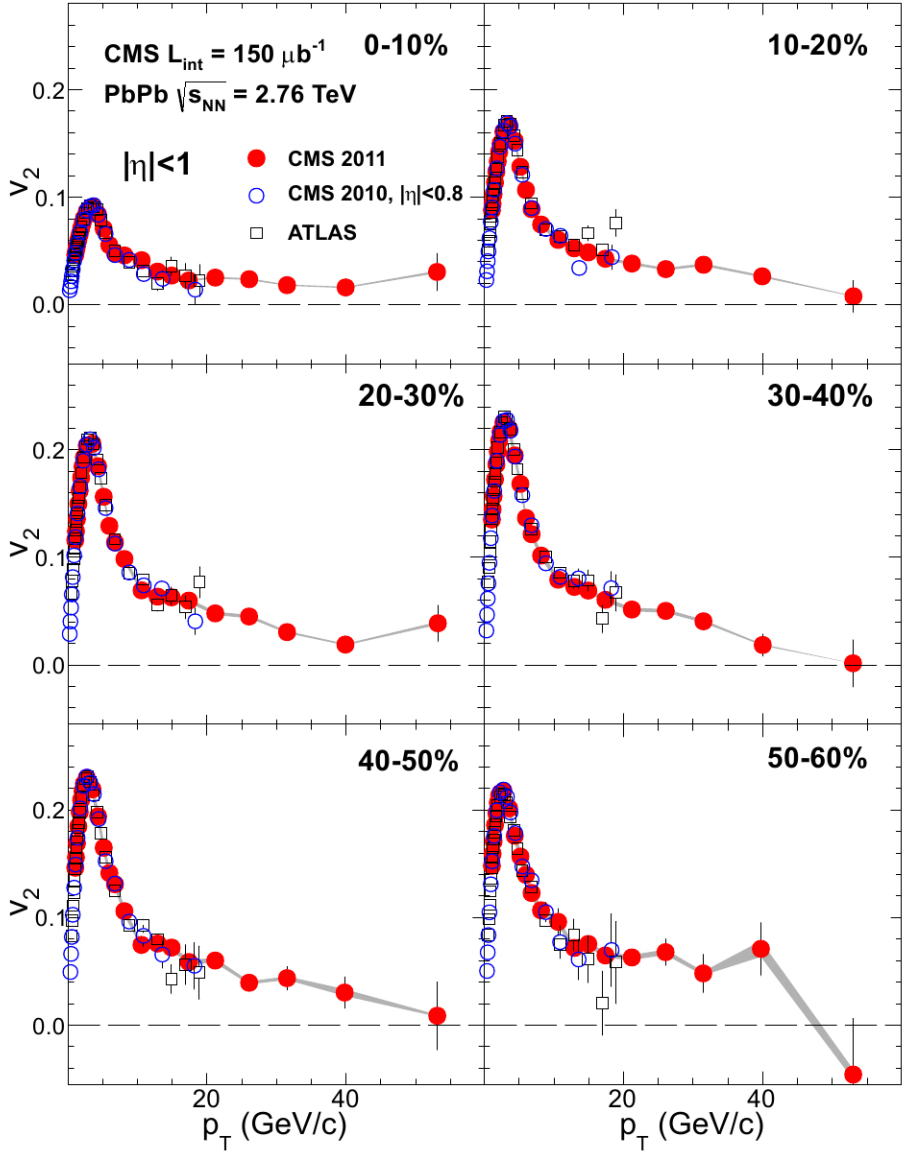


Figure 10: Elliptic flow, v_2 , as a function of the charged particle transverse momentum from 1 to 60 GeV/c with $|\eta| < 1$ for six centrality ranges in Pb-Pb collisions at $\sqrt{s_{NN}} = 2.76 \text{ TeV}$, measured by the CMS experiment. [59].

and Q-Pythia [68]. Other Monte Carlo models include JEWEL [69] and Ya-JEM [70].

Jet quenching in heavy-ion collisions is usually quantized with the nuclear modification factor R_{AA} , which is defined as

$$R_{AA}(p_T) = \frac{(1/N_{AA}^{evt}) dN^{AA}/dp_T}{\langle N_{coll} \rangle (1/N_{pp}^{evt}) dN^{pp}/dp_T} \quad (16)$$

where dN^{AA}/dp_T and dN^{pp}/dp_T are the yields in heavy-ion and proton-proton collisions, respectively and $\langle N_{coll} \rangle$ is the average number of binary nucleon-nucleon collisions in one heavy-ion event. The number of binary collisions can be calculated from the Glauber model as shown in Sec. 2.1.1. From the point of view of direct production a heavy-ion collision can be estimated relatively well to be only a series of proton-proton collisions.

If the medium has no effect on high p_T particles the nuclear modification factor should be 1. At RHIC and LHC this has been observed to be as low as 0.2 because of jet quenching. Measurements of R_{AA} from different sources are shown in Fig. 14

The nuclear modification factor can also be used to quantify anisotropy. In the study of anisotropy R_{AA} in-plane and out-of-plane can be compared. The distance traveled through medium is largest out-of-plane which leads to stronger suppression in this direction. The nuclear modification factor as a function of $\Delta\phi = \phi - \psi_n$ is given by

$$\begin{aligned} R_{AA}(\Delta\phi, p_T) &= \frac{(1/N_{AA}^{evt}) d^2N^{AA}/d\Delta\phi dp_T}{\langle N_{coll} \rangle (1/N_{pp}^{evt}) dN^{pp}/dp_T} \approx \frac{dN^{AA}/dp_T (1 + 2 \cdot v_2 \cos(2\Delta\phi))}{\langle N_{coll} \rangle dN^{pp}/dp_T} \\ &= R_{AA}^{incl}(p_T) (1 + 2 \cdot v_2 \cos(2\Delta\phi)). \end{aligned} \quad (17)$$

The yield of proton-proton collisions is independent of the reaction plane and the yield in heavy-ion collisions is modulated by the second harmonics. In Eq. (22) R_{AA} is approximated only up to the second harmonics. From Eq. (22) it follows that

$$\frac{R_{AA}(0, p_T) - R_{AA}(\pi/2, p_T)}{R_{AA}^{incl}(p_T)} \approx \frac{R_{AA}^{incl}(p_T) (1 + 2 \cdot v_2 - (1 - 2 \cdot v_2))}{R_{AA}^{incl}(p_T)} = 4 \cdot v_2 \quad (18)$$

The observed $R_{AA}(\Delta\phi, p_T)$ from PHENIX measurements in Au-Au collisions at $\sqrt{s} = 200\text{GeV}$ [82] is compared to R_{AA} using v_2 via Eq. (22) in Fig. 15. They agree very well within the statistical errors for all centrality and p_T bins.

At high- p_T , the pQCD processes are dominant, hence the v_n (or $R_{AA}(\Delta\phi, p_T)$) characterize the pathlength-dependence of the energy loss process.

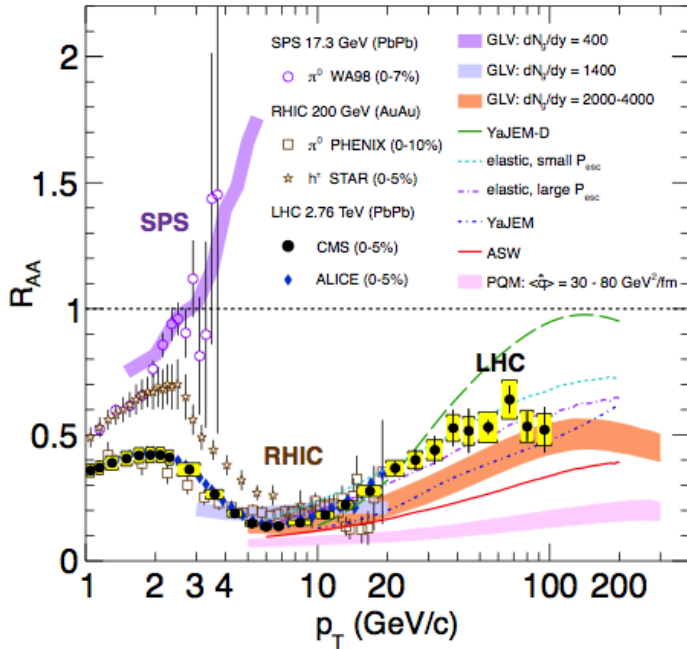


Figure 11: Measurements of the nuclear modification factor R_{AA} in central heavy-ion collisions at three different center-of-mass energies, as a function of p_T , for neutral pions (π^0), charged hadrons (h^\pm), and charged particles [71–75], compared to several theoretical predictions [32, 76–80]. The error bars on the points are the statistical uncertainties, and the yellow boxes around the CMS points are the systematic uncertainties. The bands for several of the theoretical calculations represent their uncertainties [81].

609 Jet quenching is not the only high p_T phenomenon studied in heavy-ion collisions. Another property is jet fragmentation. The high momentum parton created
 610 in the initial collision fragments into a number of partons with smaller p_T . Jet
 611 fragmentation occurs also in proton-proton collisions in the vacuum, but it can
 612 be modified due to the presence of the medium. In order to study the jet frag-
 613 mentation function ($D(z)$, where $z = p_T^h/p_T^{part}$) modification due the medium, we
 614 use the two-particle correlations. The particle yield can be extracted from the
 615 correlation function. The background from the flow processes is correlated and
 616 needs to be subtracted to get the particle yield associated only with the jet. The
 617 ratio of the jet yields in Au-Au and p-p collision $I_{AA} = Y^{Au+Au}/Y^{p+p}$ character-
 618 izes the jet fragmentation modification [83]. I_{AA} probes the interplay between the
 619 parton production spectrum, the relative importance of quark-quark, gluon-gluon
 620 and quark-gluon final states, and energy loss in the medium.

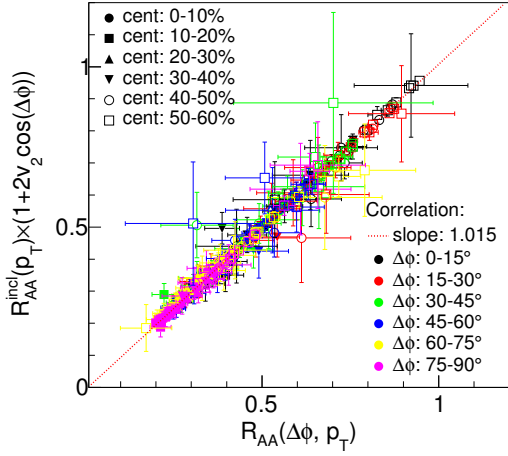


Figure 12: A comparison between observed $R_{AA}(\Delta\phi, p_T)$ and R_{AA} using v_2 from PHENIX measurements of Au-Au collisions at $\sqrt{s} = 200\text{GeV}$. On the X-axis is the measured $R_{AA}(\Delta\phi, p_T)$. On the y-axis is the inclusive R_{AA} multiplied by $1 + 2v_2 \cos(\Delta\phi)$ [82].

622 2.4 Hard processes

623 2.4.1 Jet fragmentation

624 Jet fragmentation can be factorised into three components; the parton distribution
 625 functions f_a , f_b that give the probability of getting a parton with momentum
 626 fraction x of the proton, the cross section of the elementary scattering $ab \rightarrow cd$
 627 and the fragmentation functions that give the probability of getting hadron h from
 628 the parton.

629 -Explain Parton distribution functions

$$x_a = \frac{|p_a|}{|p_{proton}|}$$

$$\frac{d\sigma_{pp}^h}{dy d^2p_T} = K \sum_{abcd} \int dx_a dx_b f_a(x_a, Q^2) f_b(x_b, Q^2) \frac{d\sigma}{dt} (ab \rightarrow cd) \frac{D_{h/c}^0}{\pi z_c}$$

630 2.4.2 Jet hadronisation

631 When the parton shower reaches a scale close to Λ_{QCD} , the perturbative description
 632 is no longer valid. Thus the hadronization stage must be described in a non-
 633 perturbative manner.

634 -Local parton-hadron duality [?]

635 Hadronisation is assumed to be universal, i.e. it shouldn't depend on the
636 collision energy or system.

637 2.4.3 Jet energy loss

638 High momentum particles are very rare and they are only produced in the ini-
639 tial collisions. After they are created they escape the medium before a thermal
640 equilibrium is reached. Thus they are not part of the pressure-driven collective
641 expansion. Instead high momentum yield is suppressed because of energy loss in
642 the medium. When propagating through the medium these partons lose energy as
643 they pass through the medium. This is referred to as jet quenching. Jet quenching
644 depends on the path lengths through the medium. Thus anisotropy in this region
645 is mainly dependent on the collision geometry and density of medium.

646 The energy loss of partons in medium is mainly due to QCD bremsstrahlung
647 and to elastic scatterings between the parton and the medium.

648 In elastic scatterings the recoil energy of the scattered partons are absorbed
649 by the thermal medium, which reduces the energy of the initial parton. The mean
650 energy loss from elastic scatterings can be estimated by

$$\langle \Delta E \rangle_{el} = \sigma \rho L \langle E \rangle_{1scatt} \propto L, \quad (19)$$

651 where σ is the interaction cross section and $\langle E \rangle_{1scatt}$ is the mean energy transfer
652 of one individual scattering [60].

653 Another energy loss mechanism is medium-induced radiation. In QCD this
654 radiation is mainly due to the elementary splitting processes, $q \rightarrow qg_r$ and $g \rightarrow gg_r$.
655 Assuming that the parton is moving with the speed of light radiation energy loss
656 can be estimated by

$$\langle \Delta E \rangle_{rad} \propto T^3 L^2, \quad (20)$$

657 where L is the length of the medium and T is its temperature [61].

658 There are several models that attempt to describe the nature of the energy loss
659 mechanism. The most used models can be divided into four formalisms.

660 In the Gyulassy-Levai-Vitev (GLV) [62] opacity expansion model the radiative
661 energy loss is considered on a few scattering centers N_{scatt} . The radiated gluon
662 is constructed by pQCD calculation as summing up the relevant scattering am-
663 plitudes in terms of the number of scatterings. Another approach into opacity
664 expansion is the ASW model by Armesto, Salgado and Wiedermann [63].

665 Thermal effective theory formulation by Arnold, Moore and Yaffe (AMY) [64]
666 uses dynamical scattering centers. It is based on leading order pQCD hard thermal

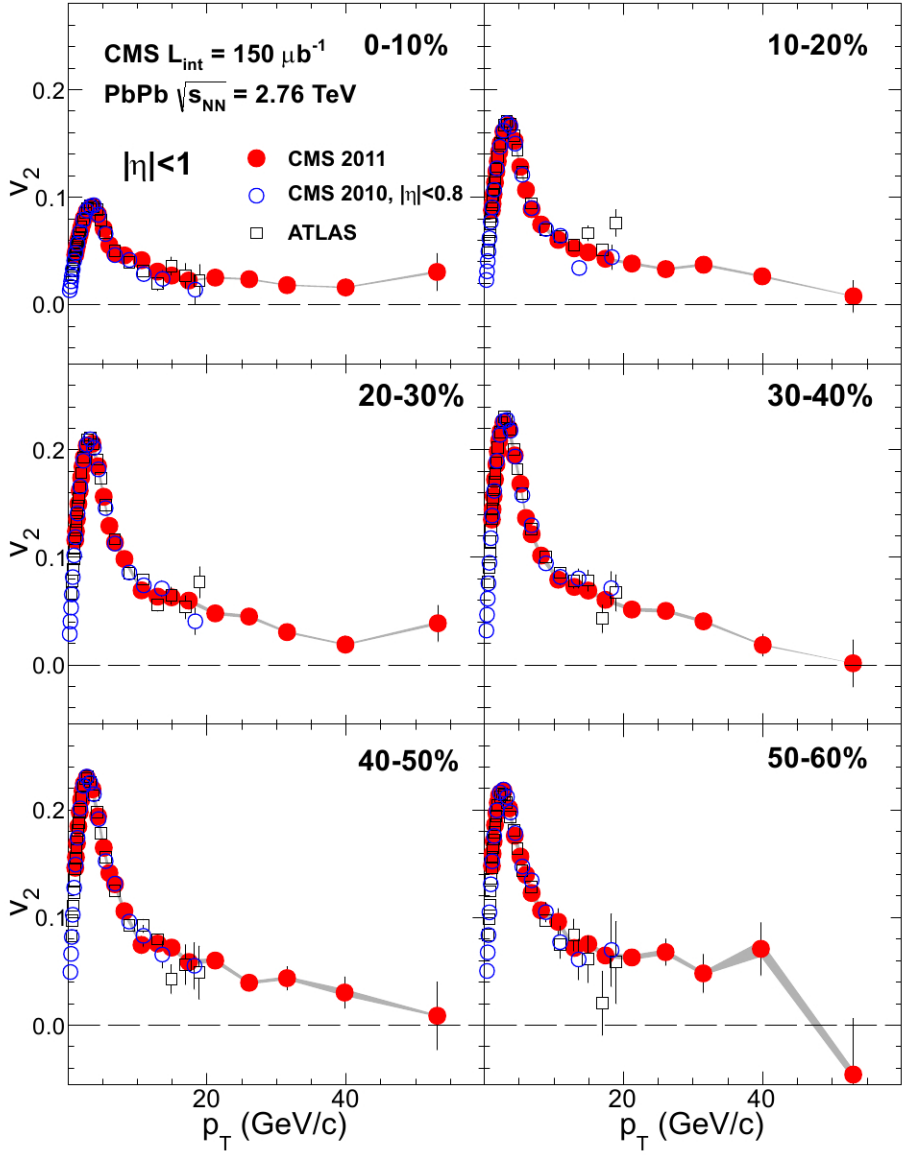


Figure 13: Elliptic flow, v_2 , as a function of the charged particle transverse momentum from 1 to 60 GeV/c with $|\eta| < 1$ for six centrality ranges in Pb-Pb collisions at $\sqrt{s_{NN}} = 2.76 \text{ TeV}$, measured by the CMS experiment. [59].

loop effective field theory. This model assumes that because of the high temperature of the plasma the strong coupling constant can be treated as small. The parton propagating through the medium will lose energy from soft scatterings and hard scatterings.

The above models calculate the energy loss while the parton propagates through the medium, focusing on the pQCD part. The higher twist (HT) approach by Wang and Guo [65] implements the energy loss mechanism in the energy scale evolution of the fragmentation functions.

The last category is formed by the Monte Carlo methods. The PYTHIA event generator [66] is widely used in high-energy particle physics. Two Monte Carlo models based on PYTHIA describing the energy loss mechanism are PYQUEN [67] and Q-Pythia [68]. Other Monte Carlo models include JEWEL [69] and YaJEM [70].

Jet quenching in heavy-ion collisions is usually quantized with the nuclear modification factor R_{AA} , which is defined as

$$R_{AA}(p_T) = \frac{(1/N_{AA}^{evt}) dN^{AA}/dp_T}{\langle N_{coll} \rangle (1/N_{pp}^{evt}) dN^{pp}/dp_T} \quad (21)$$

where dN^{AA}/dp_T and dN^{pp}/dp_T are the yields in heavy-ion and proton-proton collisions, respectively and $\langle N_{coll} \rangle$ is the average number of binary nucleon-nucleon collisions in one heavy-ion event. The number of binary collisions can be calculated from the Glauber model as shown in Sec. 2.1.1. From the point of view of direct production a heavy-ion collision can be estimated relatively well to be only a series of proton-proton collisions.

If the medium has no effect on high p_T particles the nuclear modification factor should be 1. At RHIC and LHC this has been observed to be as low as 0.2 because of jet quenching. Measurements of R_{AA} from different sources are shown in Fig. 14

The nuclear modification factor can also be used to quantify anisotropy. In the study of anisotropy R_{AA} in-plane and out-of-plane can be compared. The distance traveled through medium is largest out-of-plane which leads to stronger suppression in this direction. The nuclear modification factor as a function of $\Delta\phi = \phi - \psi_n$ is given by

$$\begin{aligned} R_{AA}(\Delta\phi, p_T) &= \frac{(1/N_{AA}^{evt}) d^2N^{AA}/d\Delta\phi dp_T}{\langle N_{coll} \rangle (1/N_{pp}^{evt}) dN^{pp}/dp_T} \approx \frac{dN^{AA}/dp_T (1 + 2 \cdot v_2 \cos(2\Delta\phi))}{\langle N_{coll} \rangle dN^{pp}/dp_T} \\ &= R_{AA}^{inel}(p_T) (1 + 2 \cdot v_2 \cos(2\Delta\phi)). \end{aligned} \quad (22)$$

The yield of proton-proton collisions is independent of the reaction plane and the yield in heavy-ion collisions is modulated by the second harmonics. In Eq. (22)

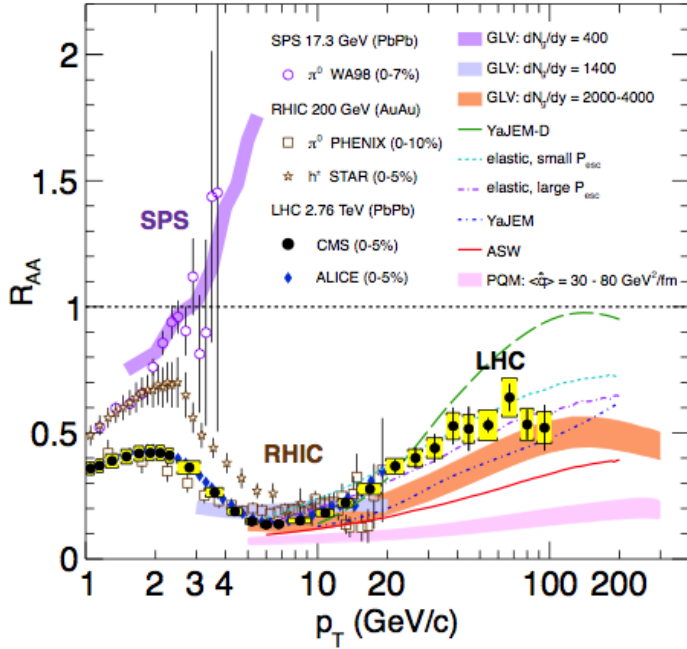


Figure 14: Measurements of the nuclear modification factor R_{AA} in central heavy-ion collisions at three different center-of-mass energies, as a function of p_T , for neutral pions (π^0), charged hadrons (h^\pm), and charged particles [71–75], compared to several theoretical predictions [32, 76–80]. The error bars on the points are the statistical uncertainties, and the yellow boxes around the CMS points are the systematic uncertainties. The bands for several of the theoretical calculations represent their uncertainties [81].

698 R_{AA} is approximated only up to the second harmonics. From Eq. (22) it follows
699 that

$$\frac{R_{AA}(0, p_T) - R_{AA}(\pi/2, p_T)}{R_{AA}^{incl}(p_T)} \approx \frac{R_{AA}^{incl}(p_T) (1 + 2 \cdot v_2 - (1 - 2 \cdot v_2))}{R_{AA}^{incl}(p_T)} = 4 \cdot v_2 \quad (23)$$

700 The observed $R_{AA}(\Delta\phi, p_T)$ from PHENIX measurements in Au-Au collisions at
701 $\sqrt{s} = 200\text{GeV}$ [82] is compared to R_{AA} using v_2 via Eq. (22) in Fig. 15. They
702 agree very well within the statistical errors for all centrality and p_T bins.

703 At high- p_T , the pQCD processes are dominant, hence the v_n (or $R_{AA}(\Delta\phi, p_T)$)
704 characterize the pathlength-dependence of the energy loss process.

705 Jet quenching is not the only high p_T phenomenon studied in heavy-ion colli-
706 sions. Another property is jet fragmentation. The high momentum parton created
707 in the initial collision fragments into a number of partons with smaller p_T . Jet

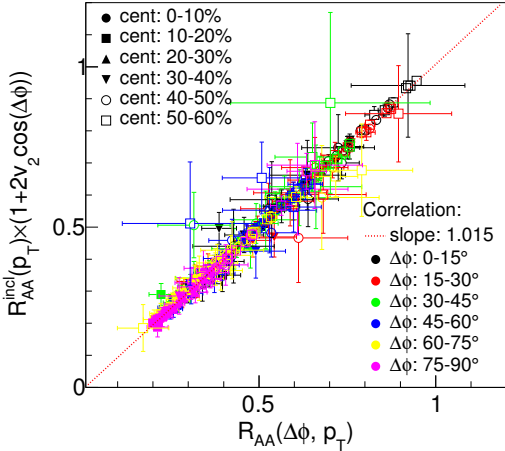


Figure 15: A comparison between observed $R_{AA}(\Delta\phi, p_T)$ and R_{AA} using v_2 from PHENIX measurements of Au-Au collisions at $\sqrt{s} = 200\text{GeV}$. On the X-axis is the measured $R_{AA}(\Delta\phi, p_T)$. On the y-axis is the inclusive R_{AA} multiplied by $1 + 2v_2 \cos(\Delta\phi)$ [82].

708 fragmentation occurs also in proton-proton collisions in the vacuum, but it can
 709 be modified due to the presence of the medium. In order to study the jet frag-
 710 mentation function ($D(z)$, where $z = p_T^h/p_T^{part}$) modification due the medium, we
 711 use the two-particle correlations. The particle yield can be extracted from the
 712 correlation function. The background from the flow processes is correlated and
 713 needs to be subtracted to get the particle yield associated only with the jet. The
 714 ratio of the jet yields in Au-Au and p-p collision $I_{AA} = Y^{Au+Au}/Y^{p+p}$ charac-
 715 terizes the jet fragmentation modification [83]. I_{AA} probes the interplay between the
 716 parton production spectrum, the relative importance of quark-quark, gluon-gluon
 717 and quark-gluon final states, and energy loss in the medium.

718 2.4.4 Monte Carlo Implementations

719 2.5 QGP in Small systems

720 After the existence of QGP in heavy ion collisions has been established, attention
 721 has been turned to small systems. Proton-proton (pp) and proton-Lead (pPb)
 722 collisions have been studied at LHC and RHIC has studied a host of different
 723 collision systems; namely proton-Gold (pAu), deuteron-Gold (dAu) and Helium³-
 724 Gold (He³Au) collisions starting in 2000.

725 Already before the era of modern colliders, collective behaviour in proton-

726 proton collisions was considered by names like Heisenberg, Fermi and Bjorken. [84]
 727 Eventually there were some experimental searches of QGP in pp and $p\bar{p}$ collisions
 728 in E735 at Tevatron [85] and MiniMAX [86]. However no conclusive evidence was
 729 found.

730 In the early years of RHIC these small systems were mostly considered as con-
 731 trol measurement, for example in constraining nuclear modified parton distribution
 732 functions (nPDFs) that determine the initial gluon distributions that determine
 733 the first epoch of heavy ion collisions [87, 88].

734 In 2010 ultrahigh-multiplicity pp collisions were studied at CMS. The study
 735 found that particles had a weak but clear preference to be emitted along a common
 736 transverse ϕ angle across all rapidities [89]. This seemed like behaviour were sim-
 737 ilar to AA collisions, but it was argued that it could as well come from momentum
 738 correlations present in the earliest moments of the collision.

739 In 2012 LHC ran its first pPb data taking period. Around the same time
 740 dAu data was reexamined at RHIC. Now it was revealed that most of the flow
 741 signatures attributed to hydrodynamic expansion in AA collisions also existed in
 742 smaller systems.

743 -Sub nucleonic structure needed to describe intial conditions in pA, pp

744 2.5.1 Collective phenomena

745 The most rugged analysis of collective behaviour concerns the two (or more) parti-
 746 cle correlations, often parametrised via the relative azimuthal angle and pseudora-
 747 pidity differences, $\Delta\phi$ and $\Delta\eta$ respectively. Figure 17 shows two-particle correla-
 748 tions measurements in PbPb, pPb and pp collisions at the LHC. In PbPb collisions

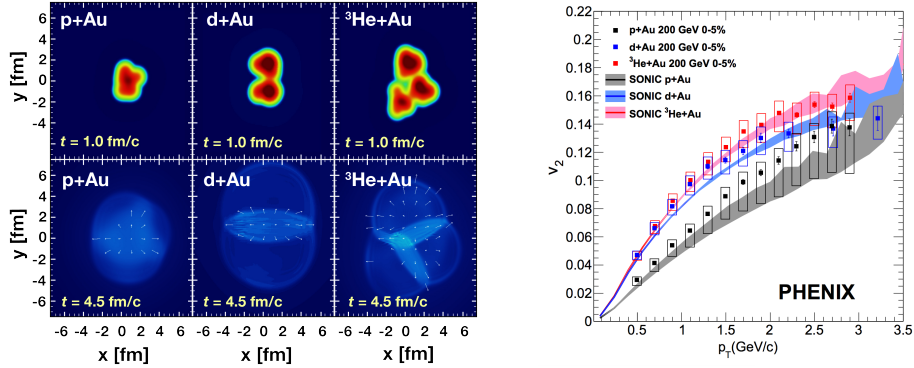


Figure 16: Calculations of the intial energy density in small collision systems at RHIC and the resulting hydrodynamic evolution.

long-range correlations dominate over short-range phenomena. This shows in the two ridges at $\Delta\phi = 0$ and $\Delta\phi = \pi$. At $\Delta\phi \approx \Delta\eta \approx 0$, there is a peak coming from single jet fragmentation. Since the away-side jet can be spread out in $\Delta\eta$, this contribution disappears when compared to the flow contribution at the away side ridge. In pPb, and pp the near side peak is more distinguished and the away-side jet contribution starts to show. Still, one can see long-range correlations that seem like flow-like collective behaviour in both systems.

In addition to the two particle correlations, correlations have been observed in the form of v_n coefficients both at LHC and at RHIC. The results have also been described with hydrodynamical models, although the applicability of said models is questionable, because of the large Reynolds numbers in small systems. Figure 16 shows results for v_2 in different collisions systems at RHIC as measured by PHENIX. These different systems provide also different initial geometries. dAu collisions naturally have an ellipsoidal form, while a He3 collision has a triangular form and thus produces larger triangular flow, v_3 components.

Other observations that produce flow-like results include mass ordered v_2 coefficients and higher order harmonics coming from fluctuations in the initial geometry. Thus all the major collective flow phenomena observed in heavy-ion collisions have been also identified in small systems.

One open question is identifying the point where flow-like correlations end. The question has proved challenging since low multiplicity events are dominated by non-flow phenomena. This makes observations in low multiplicity events model/method dependant. Different methods assess non-flow contributions differently. Thus some methods fail to observe a signal in cases, where others do and it is unclear whether this is true collective motion or it comes from non-flow contributions.

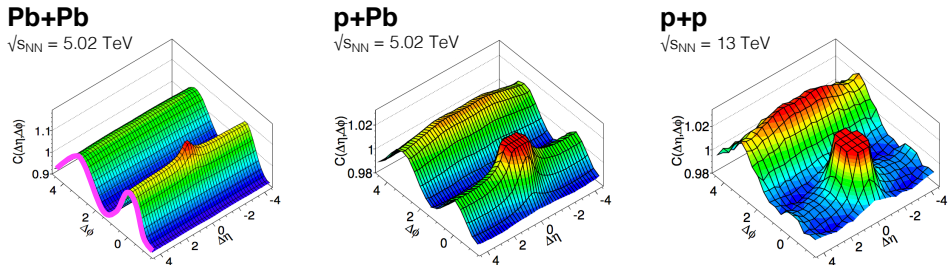


Figure 17: Two-particle correlation results in PbPb, pPb, and pp collisions at the LHC [].

775 **2.5.2 Absence of jet quenching**

776 In A+A collisions, an important confirmation of the standard model comes from
 777 the energy loss of high p_T partons traversing the medium, referred to as jet quench-
 778 ing [90–92]. In 2003 the jet quenching effect was observed to disappear in d+Au
 779 collisions. This was taken as an indication that no QGP was created. Similarly at
 780 LHC no jet modification has been observed in pPb collisions. Fig. 18 shows the
 781 nuclear modification factor R_{pA} in pPb collisions as measured at the LHC.

782 The lack of jet modification seems surprising considering the multitude of flow
 783 observations supporting the existence of QGP in small systems. One possible
 784 explanation is simply the size of medium. In PbPb collision partons traversing
 785 through the medium lose energy to the medium. If the medium is very small there
 786 is limited time for interaction with the medium.

787 Calculations indicate that there should be modification in the most central
 788 pPb collisions, but selecting these in the analysis is complicated. In PbPb colli-
 789 sions most of the particle production comes from the medium and thus the total
 790 multiplicity is a good indicator of centrality. In pPb collisions, however the total
 791 multiplicity is smaller and is more strongly influenced by jet phenomena. Events
 792 with jets have naturally larger multiplicities and are more likely to be classified as
 793 central events.

794 So far the only observable indicative of jet quenching in pPb collisions is the
 795 high $p_T v_2$. In heavy-ion collisions this is not explained by hydrodynamics. Instead
 796 it is assumed to come from jet quenching with different path lengths through the
 797 medium in different directions. In Fig.18 ATLAS and CMS measurements of v_2 in
 798 pPb and PbPb collisions are shown. The pPb results seem to follow a very similar
 799 pattern. But

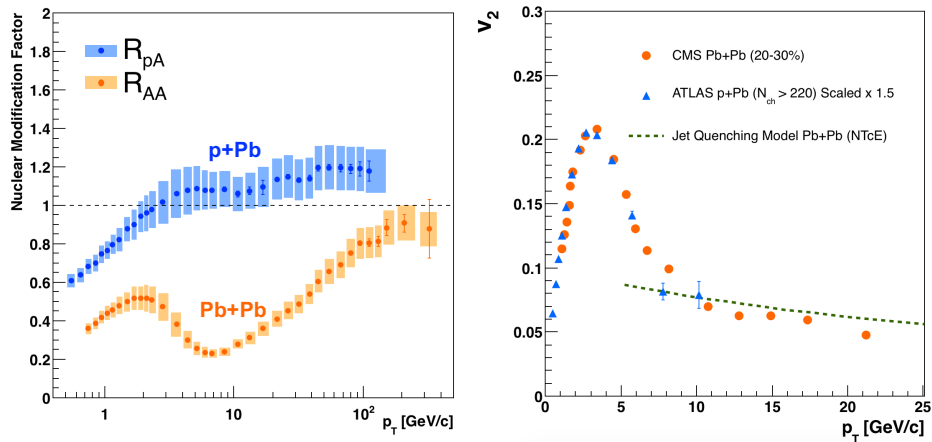


Figure 18: RpA in proton-lead collisions

Table 1: Summary of observations in small system

Observable	PbPb	pPb	pp
Jet RpA/RAA	Modified	No modification	-
Hadron RpA/RAA	Modified	No modification	-
Heavy flavors			
Jet shape	Broadening	No observations	-
Two-particle correlations	Ridge	Ridge	Ridge
v_2	Observed	Observed	Observed
Mass ordered flow			
Higher ordered harmonics			
High $p_T v_2$	Observed	Maybe	-

800 3 Experimental setup and data samples

801 The $\sqrt{s_{\text{NN}}} = 5.02$ TeV p–Pb ($1.3 \cdot 10^8$ events, $\mathcal{L}_{\text{int}} = 620 \text{ nb}^{-1}$) collisions were
802 recorded in 2013 by the ALICE detector [93]. The details of the performance of
803 the ALICE detector during LHC Run 1 (2009–2013) are presented in Ref. [94].

804 The analysis uses charged tracks that are reconstructed with the Inner Tracking
805 System (ITS) [95] and the Time Projection Chamber (TPC) [96]. These detectors
806 are located inside the large solenoidal magnet, that provides a homogeneous mag-
807 netic field of 0.5 T. Tracks within a pseudorapidity range $|\eta| < 0.9$ over the full
808 azimuth can be reconstructed. The ITS is made up of the innermost Silicon Pixel
809 Detector (SPD), the Silicon Drift Detector (SDD) and the outermost Silicon Strip
810 Detector (SSD). Each of these consists of two layers. The TPC is a cylinder filled
811 with gas. Gas is ionised along the path of charged particles. Liberated electrons
812 drift towards the end plates of the cylinder where they are detected. Combining
813 the information from the ITS and the TPC provides a resolution ranging from 1
814 to 10 % for charged particles with momenta from 0.15 to 100 GeV/c. For tracks
815 without the ITS information, the momentum resolution is comparable to that
816 of ITS+TPC tracks below transverse momentum $p_T = 10$ GeV/c, but for higher
817 momenta the resolution reaches 20 % at $p_T = 50$ GeV/c [94, 97].

818 Neutral particles used in jet reconstruction are reconstructed by the Electro-
819 magnetic Calorimeter (EMCAL) [98]. The EMCAL covers an area with a range
820 of $|\eta| < 0.7$ in pseudorapidity and 100 deg in azimuth. EMCAL is complimented
821 with the Dijet Calorimeter (DCal) [99] and Photon Spectrometer (PHOS) [100]
822 that are situated opposite of the EMCAL in azimuth. PHOS covers 70 degrees
823 in azimuth and $|\eta| < 0.12$. The DCal is technologically identical to EMCal. The
824 DCal coverage spans over 67 degrees in azimuth, but in pseudorapidity the mid
825 region is occupied by the PHOS. In between PHOS and DCal active volumes, there
826 is a gap of 10 cm. DCal is fully back-to-back with EMCal.

827 The combination of charged tracks with $p_T > 0.15$ GeV/c and neutral particles
828 with $p_T > 0.30$ GeV/c is used to construct jets.

829 The V0 detector [101] provides the information for event triggering. The V0
830 detector consists of two scintillator hodoscopes that are located on either side of
831 the interaction point along the beam direction. It covers the pseudorapidity region
832 $-3.7 < \eta < -1.7$ (V0C) and $2.8 < \eta < 5.1$ (V0A). For the 2013 p–Pb collisions
833 events are required to have signals in both V0A and V0C. This condition is used
834 later offline to reduce the contamination of the data sample from beam-gas events
835 by using the timing difference of the signal between the two stations [94].

836 EMCAL is also used to provide the jet trigger used in triggered datasets. EM-
837 CAL can be used to trigger on single shower deposits or energy deposits integrated
838 over a larger area. Latter case is used for jet triggers. The EMCAL trigger defini-
839 tion in the 2013 p–Pb collisions requires an energy deposit of either 10 GeV for the

840 low threshold trigger or 20 GeV for the high threshold trigger in a 32×32 patch
841 size.

842 In p–Pb collisions the tracks are selected following the hybrid approach [102]
843 which ensures a uniform distribution of tracks as a function of azimuthal angle
844 (φ). The momentum resolutions of the two classes of particles are comparable up
845 to $p_T \approx 10$ GeV/ c , but after that, tracks without ITS requirements have a worse
846 resolution [94, 97].

847 4 Experimental Details

848 4.1 CERN

849 The European Organization for Nuclear Research (CERN) is the largest particle
850 physics laboratory in the world. CERN was founded in 1954. In 2019 CERN
851 consists of 22 member states. Additionally CERN has contacts with a number
852 of associate member states and various individual institutions. Some 12000 vis-
853 iting scientists from over 600 institutions in over 70 countries come to CERN for
854 their research. CERN itself is located near Geneva at the border of France and
855 Switzerland and itself employs about 2500 people.

856 The laboratory includes a series of accelerators, which are used to accelerate
857 the particle beams used. A schematic view of the complex as of 2019 is shown
858 in Figure ???. In the framework of this thesis the main component is the Large
859 Hadron Collider (LHC), the largest collider at CERN. LHC will be discussed in
860 the chapter in more detail. Other accelerators in the series are used to inject the
861 particle beam into LHC, but they are also used in itself for various experimental
862 studies.

863 The second largest accelerator is the super proton synchrotron (SPS). It is final
864 step before the particle beam is injected into LHC. Commissioned in 1976, it was
865 the largest accelerator at CERN until the the Large Electron-Positron Collider
866 (LEP) was finished in 1989. Originally it was used as a proton-antiproton collider
867 and as such provided the data for the UA1 and UA2 experiments, which resulted in
868 the discovery of the W and Z bosons. At the moment there are several fixed target
869 experiments utilising the beam from SPS. These study the structure (COMPASS)
870 and properties (NA61/SHINE) of hadrons, rare decays of kaons (NA62) and radi-
871 ation processes in strong electromagnetic fields (NA63). Additionally the AWAKE
872 and UA9 experiments are used for accelerator research and development.

873 -PS

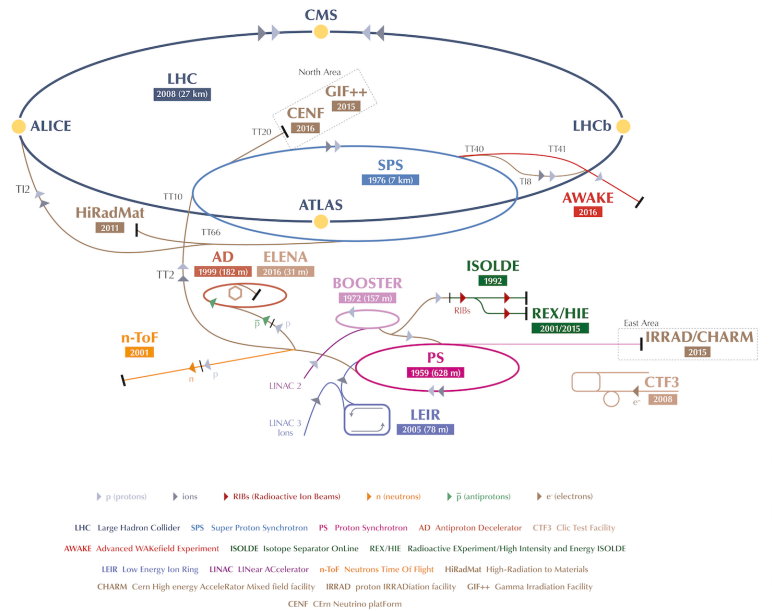


Figure 19: A schematic view of the accelerator complex at CERN. Before particles can be injected into the LHC they require a series of preliminary? acceleterarors. Until 2018 protons start their journey in LINAC2 (Linear Accelerator) and continue through the Booster, Proton Synchrotron (PS) and Super Proton Synchrotron (SPS). Between 2019 and 2020 LINAC2 will be replaced by LINAC4 [?]

874 **4.2 Large Hadron Collider**

875 The Large Hadron Collider (LHC) is the largest accelerator at CERN and the
876 largest particle collider ever built. The LHC is designed to accelerate protons
877 up to an energy of 8 TeV and lead ions up to 2.76 TeV per nucleon [?]. The design
878 luminosity of the LHC is $10^{34} \text{ cm}^{-2} \text{ s}^{-1}$. In 20xx it achieved a record peak luminosity
879 of xxx. For lead beams the design luminosity is xxx. All this is achieved with a
880 ring of 26.7 km, that consists of 1232 superconducting dipole magnets that keep
881 particles in orbit.

882 The particles are accelerated through the use of radio-frequency (RF) cavities.
883 The RF are build such that the electromagnetic waves become resonant and build
884 up inside the cavity. Charges passing through the cavity feel the overall force
885 and are pushed forward along the accelerator. As they consist of electromagnetic
886 waves, the field in the RF cavity oscillates. Thus particles must enter the cavity at
887 the correct phase of oscillation to receive a forward push. When timed correctly,
888 the particles will feel zero accelerating voltage when they have exactly the correct
889 energy. Particles with higher energies will be decelerated and particles with lower
890 energies will be accelerated. This focuses particles in distinct bunches. The RF
891 oscillation frequency at the LHC is 400.8 MHz. Thus RF "buckets" are separated
892 by 2.5 ns. However only 10 % are actually filled with particles, so the bunch
893 spacing in the LHC is 25 ns, at a bunch frequency of 40 MHz.

894 With 7 TeV proton beams the dipole magnets used to bend the beam must
895 produce a magnetic field of 8.33 T. This can be only achieved through making
896 the magnets superconducting, which requires cooling them down with helium to a
897 temperature of 1.9 K. The 1232 dipole magnets make up roughly 2/3 of the LHC
898 circumference. The remaining part is made up of RF cavities, various sensors and
899 higher multipole magnets used to keep the beam focused. The most notable of
900 these are the 392 quadrupole magnets.

901 The LHC is divided into octants, where each octant has a distinct function.
902 Octants 2 and 8 are used to inject beam into the LHC from SPS. The 2 beams
903 are crossed in octants 1,2,5 and 8. The main experiments are built around these
904 crossing points. Octants 3 and 7 are used for beam cleansing. This is achieved
905 through collimators that scatter particles with too high momentum or position
906 offsets off from the beam. The RF cavities used for acceleration are located in
907 octant 4 and octant 6 is used for dumping the beam. The beam dump is made
908 up of two iron septum magnets, one for each beam, that will kick the beam away
909 from machine components into an absorber when needed.

910 **4.2.1 LHC experiments**

911 As of 2018 there are four main experiments at the LHC; ALICE, ATLAS, CMS
912 and LHCb and three smaller ones LHCf, TOTEM and MoEDAL. ALICE will be
913 covered in section 4.3.

914 ATLAS (A Toroidal LHC ApparatuS) and CMS (Compact Muon Solenoid) are
915 the two largest experiments at the LHC. They are both multipurpose experiments
916 designed to be sensitive to many different possible new physics signals. The biggest
917 discovery made by these so far is the discovery of the Standard Model Higgs boson,
918 which was simultaneously published by the experiments in 2012 [?, ?].

919 The LHCb (LHC beauty) experiment [?] is made for studying the bottom
920 (beauty) quark. Main physics goals include measurement of the parameters of CP
921 violation with decays of hadron containing the bottom quark. One of the most
922 important results published by LHCb is the first measurement of $B_s^0 \rightarrow \mu^+ \mu^-$
923 decay, which was found to be in line with the Standard Model.

924 In addition to the four large experiments there are three smaller experiments
925 along the LHC ring. LHCf (LHC forward) is located at interaction point 1 with
926 ATLAS. It aims to simulate cosmic rays by the particles thrown forwards by the
927 collisions in ATLAS.

928 TOTEM (TOTal Elastic and diffractive cross section Measurement) is located
929 near the CMS experiment at point 5. This allows it to measure particles emerging
930 from CMS with small angles. The main goals is to measure the total, elastic and
931 inelastic cross-sections in pp collisions [?].

932 The MoEDAL (Monopole and Exotics Detector At the LHC) experiment is
933 located at the interaction point 8 together with the LHCb experiment. MoEDAL
934 tries to measure signatures of hypothetical particles with magnetic charge, mag-
935 netic monopoles.

936 **4.3 ALICE**

937 ALICE (A Large Ion Collider Experiment) [?] is the dedicated heavy ion exper-
938 iment at the LHC. ALICE was designed to cope with the expected very high
939 multiplicity environment of heavy ion collisions. The design allows measurement
940 of a large number of low momentum tracks. The different detector subsystems are
941 optimised to provide high momentum resolution and excellent particle identifica-
942 tion capabilities over a broad range of momentum.

943 A schematic view of the ALICE detector in 2018 is presented in Figure ??.
944 The detector will go through significant upgrades during Long Shutdown 2 in
945 2019-2020. As in all the major high energy physics experiments the positioning
946 of the detectors follows a layered structure. Closest to the interaction point are
947 the tracking detectors. The main task of these detectors is to locate the position

of the primary interaction vertex accurately and to record the tracks of charged particles. To achieve this they need a very good spatial resolution close to the interaction point. Tracking detectors do not significantly alter the tracks of traversing particles. Thus they can be located in the innermost layers.

Calorimeters are designed to stop any particles hitting them and use the absorption to measure the energy of the particles. Thus they must be located behind the tracking detectors. ALICE has two separate calorimeter systems, the electromagnetic calorimeters measure mainly electrons and photons, while the muon detection system measures muons.

4.3.1 Tracking

The main design guideline for the tracking detectors in ALICE was the requirement to have good track separation and high granularity in the high multiplicity environment of heavy ion collisions. Before LHC was built the wildest estimates put the particle density at 8000 charged particles per unit of rapidity [1]. In reality the particle density turned out to be significantly smaller, about 1600 charged particles per rapidity unit. [2]

The main tracking detector in ALICE is the Time Projection Chamber (TPC), discussed in more detail in section 4.3.2

Between TPC and the beam pipe there is an array of six layers of silicon detectors, called the inner tracking system (ITS) [?]. The main tasks of the ITS are to locate the primary vertex with a resolution better than $100\ \mu m$, to reconstruct the secondary vertices from decaying particles, to track and identify particles with momenta below 200 MeV and to compliment the momentum and angle measurements of TPC. During long shutdown 2 in 2019-2020 the entire ITS will be replaced [?]. As of 2018 the two innermost layers are made of the silicon pixel detector (SPD). As it's the closest detector to the interaction point it requires are very high spatial resolution. Thus the choice of pixel technology is natural. In heavy ion collisions the particle density is around 50 particles per cm^2 .

The next two layers are the silicon drift detector (SDD), which is made out of homogeneous neutron transmutation doped silicon. It is ionized when a charged particle goes through the material. The generated charge then drifts to the collection anodes, where it is measured. The maximum drift time in SDD is about 5 μs . This design gives very good multitrack capabilities and provides two out of the four dE/dx samples in the ITS.

The two remaining layers in the ITS are the silicon strip detector (SSD). The strips work in a similar way as silicon pixels, but by itself one layer only provides good resolution in one direction. Combining two crossing grids of strips provides 2 dimensional detection. Each charged particle will hit two intervening strips. The position of the hit can be deduced from the place where the strips cross each other.

987 **4.3.2 TPC**

988 Time projection chamber (TPC) is a cylindrical detector filled with $88m^3$ of
989 Ne – CO₂ (90/10 %) gas mixture. The gas is contained in a field cage that provides
990 an uniform electric field of $400V/cm$ along the z-axis (along the beam direction).
991 Charged particles traversing through the TPC volume will ionise the gas along
992 their path. This liberates electors that drift towards the end plates of the cylin-
993 der.

994 The field cage is separated into two detection volumes by the central high
995 voltage electrode. Both sides have a drift length of 2.5 m and inner/outer diameters
996 of 1.2/5 m. This means the central electrode must provide a maximum potential
997 of 100 kV to achieve the design field magnitude. The maximum time required for
998 electrons to drift through the chamber is about $90 \mu s$.

999 When electrons reach the end of the main cylinder they enter the readout
1000 chambers. The readout section of both sides consists of 18 outer chambers and
1001 18 inner chambers. Each of them are made of multiwire proportional chambers
1002 with cathode pad readout. This design is used in many TPCs before. During
1003 Long Shutdown 2 in 2019-2020, the multiwire chambers will be replaced by Gas
1004 Electron Multipliers (GEMs, see section 4.3.3).

1005 The relatively slow drift time of $90 \mu s$ is the limiting factor for the luminosity
1006 ALICE can take. The occupancy of the TPC must be kept in a manageable level.

1007 **4.3.3 TPC upgrade**

1008 **4.3.4 Particle identification**

1009 One guiding principle in the design of ALICE was to achieve good particle iden-
1010 tification over a large part of phases space and for several different particle types.
1011 In ALICE there are several detectors taking part in the identification of particles.

1012 One of the particle identification detectors is the transition radiation detector
1013 (TRD) [?]. Its main task is identifying electors with momenta larger than 1 GeV.
1014 Transition radiation is produced when highly relativistic particles traverse the
1015 boundary between to media having different dielectric constants. The average
1016 energy of the emitted photon is approximately proportional to the Lorentz factor γ
1017 of the particle, which provides an excellent way of discriminating between electrons
1018 and pion. ALICE TRD is made of a composite layer of foam and fibres. The
1019 emitted photons are then measured in six layers of Xe/CO₂ filled time expansion
1020 wire chambers.

1021 The time of flight (TOF) detector uses a very simple physics principle, i.e.
1022 calculating the velocity of the particle using the time of flight between two points.
1023 Combining this with the momentum of particle, obtained from the tracking de-
1024 tectors, one can calculate the mass of the particle, which identifies particles. The

1025 TOF detector consists of multigap resistive wire chambers. These are stacks of
1026 resistive plates spaced equally. They allow time of flight measurements in large
1027 acceptance with high efficiency and with a resolution better than 100 ps.

1028 The third specific particle identification detector is the high momentum particle
1029 identification (HMPID) detector. The HMPID uses a ring imaging Cherenkov
1030 counter to identify particles with momenta larger than 1 GeV. Particles moving
1031 through a material faster than the speed of light in the material will produce
1032 Cherenkov radiation. The velocity of the particle determines the angle at which
1033 the radiation is emitted. Measuring this angle gives the velocity of the particle.
1034 This can be again used to calculate the mass of the particle, if the momentum is
1035 known. In HMPID the material is a liquid radiator and the photons are measured
1036 with multiwire proportional chambers in conjunction with photocathodes.

1037 -TRD
1038 -TOF
1039 -HMPID
1040 -TPC and dE/dx

1041 4.3.5 Electromagnetic Calorimeter

1042 Calorimeters are designed to measure the energy of particles. Electromagnetic
1043 calorimeters specialise in detecting particles that interact primarily through the
1044 electromagnetic interaction, namely photons and electrons. They are required in
1045 many neutral meson and direct photon analyses. In addition the energy informa-
1046 tion enhance jet measurements.

1047 ALICE has two electromagnetic calorimeters, the photon spectrometer (PHOS) [?]
1048 and the electromagnetic calorimeter (EMCal) [?]. PHOS is a homogeneous calorime-
1049 ter that consists of scintillating PbWO₄ crystals, which generate a bremsstrahlung
1050 shower and produce scintillation light. The energy of the particle determines the
1051 amount of light produced. To improve the charged particle rejection, PHOS in-
1052 cludes a charged particle veto detector (CPV) [?]. PHOS is built to have a very
1053 fine granularity, making it well suited for measuring direct photons and neutral
1054 mesons.

1055 EMCal is a sampling calorimeter. It consists of layers of lead and scintillator
1056 tiles. The lead tiles produce the shower and scintillator tiles the light. The sig-
1057 nal is then read with wavelength shifting fibres. The acceptance of EMCal in the
1058 azimuthal angle is $80 \text{ deg} < \phi < 187 \text{ deg}$. During long shutdown 1 in 2013-2015,
1059 EMCal was extended with the di-jet calorimeter (DCal) [?], giving an additional
1060 acceptance region of $260 \text{ deg} < \phi < 320 \text{ deg}$. This provides partial back-to-back
1061 coverage. In comparison to PHOS, EMCal has coarser granularity, but a signifi-
1062 cantly larger acceptance, making it suitable for jet physics.

₁₀₆₃ 4.3.6 Forward detectors

₁₀₆₄ 4.3.7 Muon spectrometer

₁₀₆₅ 4.3.8 Trigger

1066 **5 Event and track selection**

1067 **6 Analysis method**

1068 **6.1 Jet Finding**

1069 The analysis is performed by analysing jet constituents. In each collision event, the
1070 jets are reconstructed using FastJet [103] with the anti- k_T algorithm [104]. Jets for
1071 $R=0.4$ are selected in $|\eta| < 0.25$ to satisfy the fiducial acceptance of the EMCAL. In
1072 jet reconstruction both charged tracks with $p_T > 0.15 \text{ GeV}/c$ and neutral cluster
1073 with $p_T > 0.30 \text{ GeV}/c$ are considered. In the analysis, results are presented in
1074 terms of the jet transverse momentum $p_{T,\text{jet}}$.

1075 **6.1.1 Anti k_T algorithm**

1076 Jets are reconstructed using the anti- k_T algorithm [104]. The algorithm works by
1077 trying to undo the splittings through combining pseudojets/tracks.

$$k_{T,i}^2 = p_{T,i}^{2p}$$

1078 For each pair of protojets the distance measure is calculated as

$$k_{T,(i,j)}^2 = \min(p_{T,i}^{2p}, p_{T,j}^{2p}) \frac{\Delta R_{i,j}^2}{D^2},$$

1079 where

$$R_{i,j} = (\phi_i - \phi_j)^2 + (y_i - y_j)^2$$

1080 If $k_{T,i}$ is the smallest quantity then the protojet is a jet and it is removed
1081 from further consideration. If $k_{T,(i,j)}$ is the smallest quantity the two protojets are
1082 merged. Iterate until no protojets are left.

1083 The choice of the power p in the distance measure depends on the algorithm
1084 used

- 1085 • $p = 1$: k_T algorithm
- 1086 • $p = 0$: Cambridge Aachen algorithm
- 1087 • $p = -1$: anti- k_T algorithm

1088 With the choice $p = -1$ in anti- k_T algorithm, the softest splittings are undone
1089 first.

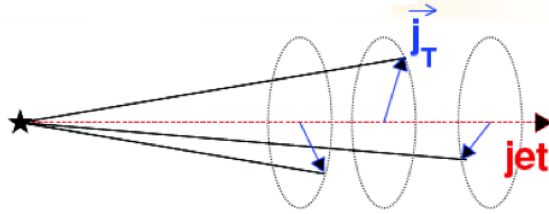


Figure 20: Illustration of \vec{j}_T . The jet fragmentation transverse momentum, \vec{j}_T , is defined as the transverse momentum component of the track momentum, \vec{p}_{track} , with respect to the jet momentum, \vec{p}_{jet} .

1090 6.2 j_T

1091 The jet fragmentation transverse momentum, j_T , is defined as the component of
 1092 the constituent particle momentum, \vec{p}_a , transverse to the jet momentum, \vec{p}_{jet} . The
 1093 resulting \vec{j}_T is illustrated in Fig. 20. The length of the \vec{j}_T vector is

$$j_T = \frac{|\vec{p}_{\text{jet}} \times \vec{p}_{\text{track}}|}{|\vec{p}_{\text{jet}}|}. \quad (24)$$

1094 It is commonly interpreted as a transverse kick with respect to the initial hard
 1095 parton momentum that is given to a fragmenting particle during the fragmentation
 1096 process, which is a measure of the momentum spread of the jet fragments [].

1097 The reconstructed jet axis is used for j_T reference. Any charged track within
 1098 a fixed cone with radius R is taken as a jet constituent, as opposed to using the
 1099 constituent list provided by the jet algorithm. Anti- k_T produces jets that are
 1100 very circular in shape. Thus this doesn't change the constituent list considerably.
 1101 Neutral tracks are used only in jet reconstruction.

1102 6.2.1 1 over j_T

j_T results are shown as

$$\frac{1}{j_T} \frac{dN}{dj_T}$$

1103 distributions. The logic behind this is that j_T is inherently a two-dimensional
 1104 observable, comprised of j_{Tx} and j_{Ty} components. So the actual physical observable
 1105 would be

$$\frac{d^2N}{dj_{Tx} dj_{Ty}}$$

1106 Changing into polar coordinates with $j_{\text{Tr}} = j_{\text{T}}$ and θ gives

$$\frac{d^2N}{j_{\text{T}} dj_{\text{T}} d\theta},$$

1107 where j_{T} over the azimuth θ should stay constant and it can be integrated over
1108 giving

$$\frac{1}{2\pi} \frac{dN}{j_{\text{T}} dj_{\text{T}}}.$$

1109 6.3 Unfolding

1110 Extend unfolding

1111 The resulting j_{T} distributions are corrected for the detector inefficiency using
1112 the unfolding method. The response matrix for the unfolding is obtained from a
1113 PYTHIA [105] simulation.

Measured distributions are affected by two main factors; Limited acceptance -
The probability to observe a given event is less than one and limited resolution -
Quantity x cannot be determined exactly, but there is a measurement error. True
 $f(x)$ and measured $g(y)$ distributions are connected by a convolution integral.
Including statistical fluctuations this becomes

$$\hat{g}(y) = \int_a^b A(y, x) f(x) dx + \epsilon(y),$$

where A is the detector response obtained by Monte Carlo simulations and $\epsilon(y)$
is the term coming from statistical fluctuations. If x and y are discrete variables
we have

$$\hat{g}_i = \sum_{j=1}^m A_{ij} f_j + \epsilon_i,$$

Or in matrix form

$$\hat{g} = Af + \epsilon$$

If the only detector effect is limited acceptance, A is a diagonal matrix. In a
general discrete case the (naive) solution is obtained by the inverse matrix

$$\hat{f} = A^{-1} \hat{g}$$

1114 However this usually leads to oscillating solutions and determining the inverse
1115 matrix can be difficult.

1116 Two common methods to perform this inversion are Bayesian and SVD unfold-
1117 ing methods. Often the solution requires some additional *a priori*. For example
1118 the solution should be smooth in most cases.

1119 **6.3.1 Bayesian unfolding**

The bayesian (iterative) method is based on the Bayes formula [].

$$P(C_i|E_j) = \frac{P(E_j|C_i) P_0(C_i)}{\sum_{l=1}^{n_C} P(E_j|C_l) P_0(C_l)},$$

1120 i.e. Probability of Cause ("truth") C_i given Effect ("observed") E_j is proportional to the probability of observing E_j given C_i (response matrix) and the truth distribution $P_0(C_i)$.

At first P_0 is given some starting distribution, either a uniform distribution or some guess of the final distribution. Taking into account the inefficiency this gives

$$\hat{n}(C_i) = \frac{1}{\epsilon_i} \sum_{j=1}^{n_E} n(E_j) P(C_i|E_j),$$

where

$$P(C_i|E_j) = \frac{P(E_j|C_i) P_0(C_i)}{\sum_{l=1}^{n_C} P(E_j|C_l) P_0(C_l)},$$

and

$$\hat{n}(C_i) = \frac{1}{\epsilon_i} \sum_{j=1}^{n_E} n(E_j) P(C_i|E_j).$$

First $P(C_i|E_j)$ is calculated with the uniform distribution or best guess of the shape of the distribution. This is then used to calculate the new distribution $\hat{P}(C_i)$

$$\hat{N}_{true} = \sum_{i=1}^{n_C} \hat{n}(C_i), \hat{P}(C_i) = P(C_i|n(E)) = \frac{\hat{n}(C_i)}{\hat{N}_{true}}$$

1123 P_0 is then replaced with \hat{P} and the procedure is repeated until an acceptable 1124 solution is found.

1125 **6.3.2 Toy Monte Carlo**

remove? A toy Monte Carlo simulation was performed to see the performance in an ideal case. Sample jet p_T values from observed p_T distribution. Starting from this p_T start creating tracks with

$$p_{track} = z_{track} p_{T,jet}$$

1126 where z_{track} is sampled from the observed z distribution. All tracks below 0.15GeV 1127 are discarded. Sampling is continued until the sum of the track transverse momenta

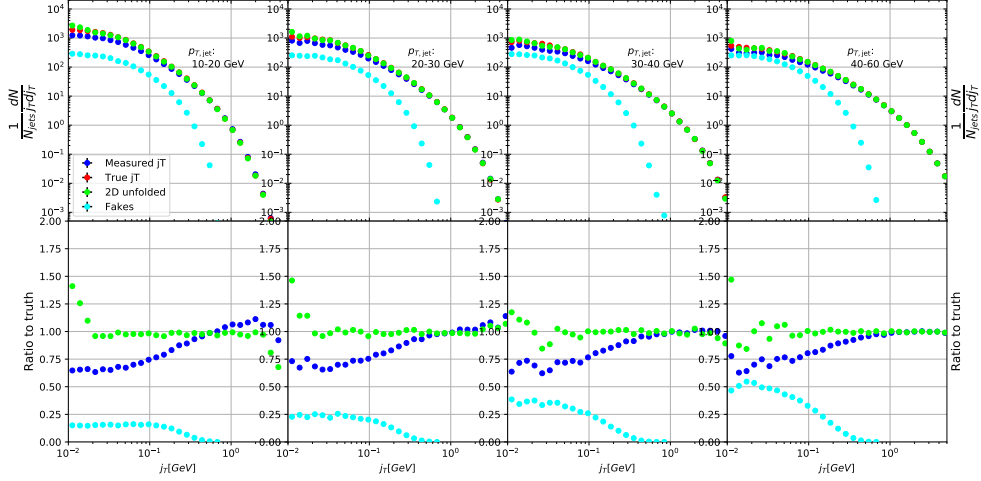


Figure 21: Results from unfolding in Toy Monte Carlo

1128 exceeds the jet transverse momentum. Jet is then defined as the sum of the track
 1129 momenta.

1130 Simultaneously a p_T dependant observation efficiency is applied to the tracks
 1131 and a separate observed jet is calculated using only the observed tracks. Addi-
 1132 tionally a set of fake tracks is added to the observed jet. Tracks are always either
 1133 observed or not at the true momentum. No smearing is added to the observed
 1134 momentum.

Afterwards the tracks are looped over for j_T calculation. For observed tracks we calculate j_T with respect to both the true jet axis and the observed jet. 2D Response matrix is filled with

$$(j_{T,\text{obs}}, p_{T,\text{jet},\text{obs}}, j_{T,\text{true}}, p_{T,\text{jet},\text{true}})$$

1135 In practice this is done with a set of 3D histograms, where $p_{T,\text{jet},\text{true}}$ determines
 1136 the histogram index and the remaining three values the bin in the 3D histogram.

1137 After creating the response matrices, an identical procedure is carried out the
 1138 create testing data. Now instead of filling response matrices, 2D histograms are
 1139 filled with $(j_{T,\text{obs}}, p_{T,\text{jet},\text{obs}})$ and $(j_{T,\text{true}}, p_{T,\text{jet},\text{true}})$

1140 The observed distributions are unfolded using RooUnfold's 2D Bayesian (iter-
 1141 ative) algorithm. Results are shown in figure 21.

1142 6.3.3 Pythia Response matrices

1143 Response matrices are filled through correlation between MC detector and particle
 1144 level jets and tracks.

Table 2: j_T and p_T ranges used in unfolding. The same ranges are used for detector and truth level.

	j_T	$p_{T\text{jet}}$
Min	0.01	5
Max	20	500

The ranges of both j_T and $p_{T\text{jet}}$ extend the ranges in end results. These are shown in Tab. 2. The ranges are the same in detector and particle level.

When calculating j_T for MC particles the code checks whether a corresponding detector level track exists and if that track had a j_T value. Additionally check for detector level tracks that don't have corresponding particle level track or that track does not have j_T value.

Possible cases:

- We find a corresponding track with a j_T value, response matrix is filled normally with $(j_T^{obs}, p_T^{obs}, j_T^{true}, p_T^{true})$
- We don't find a corresponding track. Record (j_T^{true}, p_T^{true}) as a miss
- We find a corresponding track, but it didn't have j_T value. Most likely because it was not part of a jet. Similary record (j_T^{true}, p_T^{true}) as a miss
- For detector level tracks with no correspondence in particle level set record cord (j_T^{obs}, p_T^{obs}) as a fake

6.3.4 2D response matrices

In the analysis code the response matrix is made of an array of 3 dimensional histograms, with $(j_{T,obs}, p_{T,obs}, j_{T,true})$ as axes. The histogram index gives the $p_{T,true}$ value.

6.3.5 Unfolding algorithm

As a primary method unfolding is performed with an iterative (bayesian) algorithm using the RooUnfold [106] package. The number of iterations used is 4.

6.3.6 Effect of number of iterations

The iterative unfolding algorithm permits the change of number of iterations. The unfolding was carried out using different numbers of iterations. The results from these different cases are shown in Fig. 22. The results are compared to the default unfolding algorithm with 4 iterations. The difference in results between the different cases is mostly less than 2.5%.

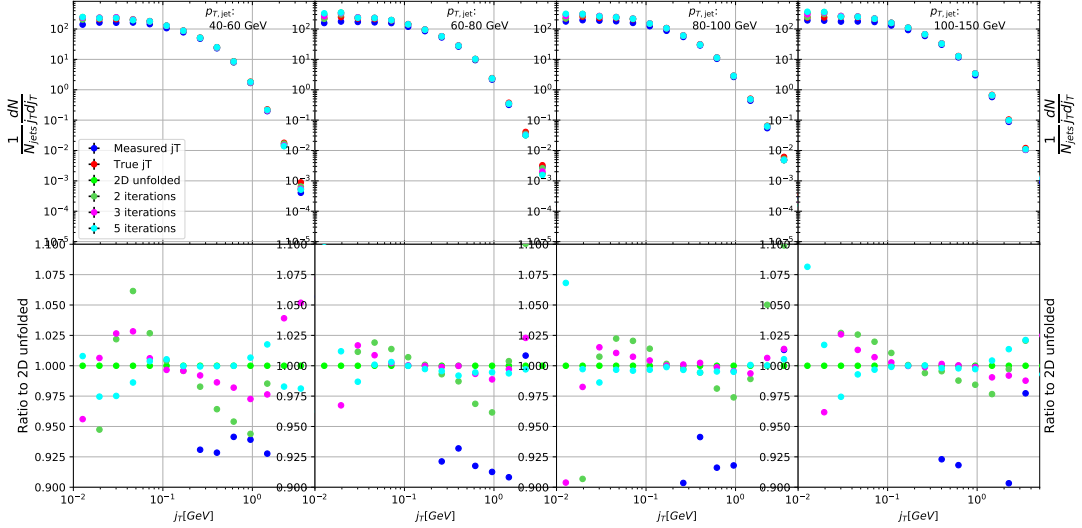


Figure 22: Unfolding with different number of iterations

1172 6.3.7 Effect of different prior

1173 The iterative algorithm requires a prior estimate of the shape of the distribution.
 1174 As a default prior the truth (particle level) distribution is used. To test the effect
 1175 of changing the prior we instead use the unfolded j_T distribution as prior. The
 1176 results are compared to the unfolding algorithm with the default prior. This is
 1177 shown in Fig. 23 The difference in results between the different cases is mostly less
 1178 than 2.5%.

1179 6.3.8 Effect of p_T truncation

1180 6.3.9 Unfolding closure test

1181 Pythia set is divided in 2 halves. First is used to fill the response matrices, as well
 1182 as record missed and fake tracks. Second half is used to test the effectiveness of
 1183 the unfolding method. Jet p_T distributions are shown in figure 25a and response
 1184 matrix are shown in figure 25b.

1185 Response matrices within single jet p_T bins are shown in figure 26. Results
 1186 from the closure test are shown in figure 27. In the lowest jet p_T bins unfolding
 1187 fails to recover the true distribution. The lowest jet p_T bins are dominated by
 1188 combinatorial jets and thus the true detector response is likely not retrieved.

1189 Above jet p_T 30-40 GeV the distribution is recovered well in the mid j_T region.
 1190 At $j_T < 0.1$ there is clear discrepancy. The final results are shown only for $j_T > 0.1$.
 1191 Additionally there is some discrepancy at very high j_T . This is taken into account

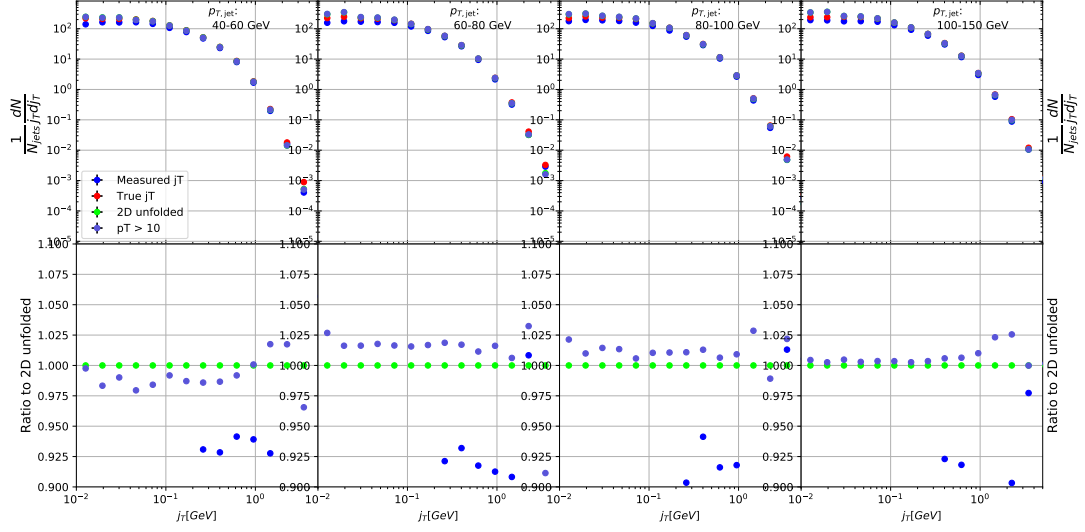


Figure 23: Effect of changing minimum jet p_T used in unfolding from 5 to 10 GeV

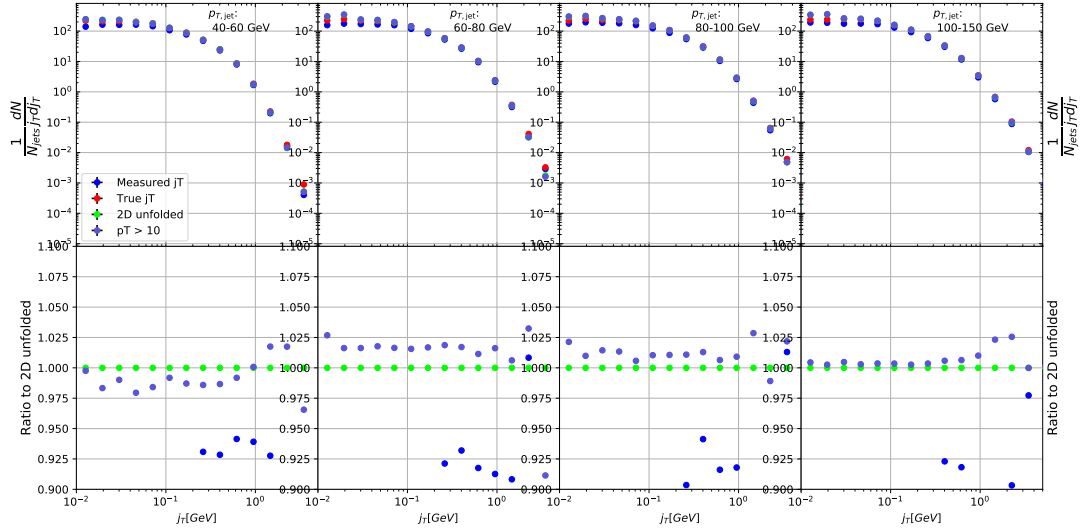
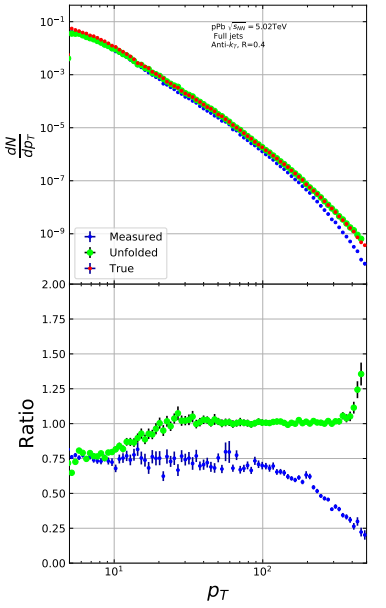
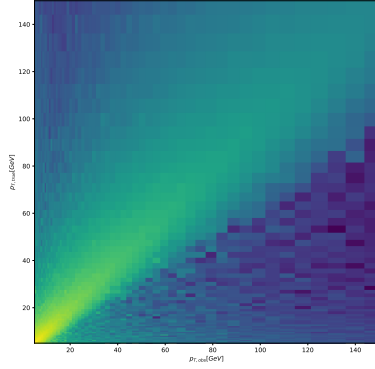


Figure 24: Effect of changing minimum jet p_T used in unfolding from 5 to 10 GeV



(a) Unfolded jet p_T distribution in Pythia closure test



(b) Jet p_T response matrix from unfolding closure test

1192 in the unfolding systematics. (TODO: Show this)

1193 6.4 Background

1194 When calculating j_T distribution for jet constituents there is a contribution from
 1195 underlying event (UE), i.e. tracks that just happen to be close to the jet axis.
 1196 To find the signal coming from the actual jet we need to subtract the background
 1197 (UE) contribution. On a jet-by-jet basis this is impossible, so we try to estimate
 1198 the background by looking at regions of the detector where there are no tracks
 1199 from jets, but only uncorrelated tracks from the underlying event.

1200 The underlying event is estimated by looking at an imaginary jet cone perpen-
 1201 dicular to the observed jet axis ($\frac{\pi}{2}$ Rotation in ϕ). j_T is calculated for any tracks
 1202 found within this cone. The vector sum of the individual track momentum and
 1203 the imaginary jet axis is used as reference for j_T . The background obtained in
 1204 this manner is subtracted from the unfolded inclusive j_T distribution, which gives
 1205 the resulting signal distribution. To make sure there is no jet contribution in the
 1206 background, any events with jets inside the perpendicular cone are not used for
 1207 background estimation.

1208 We have two methods for background estimation. In the first we look at the
 1209 direction perpendicular to the jet. This is assumed to be the region least likely to
 1210 contain jet contributions.

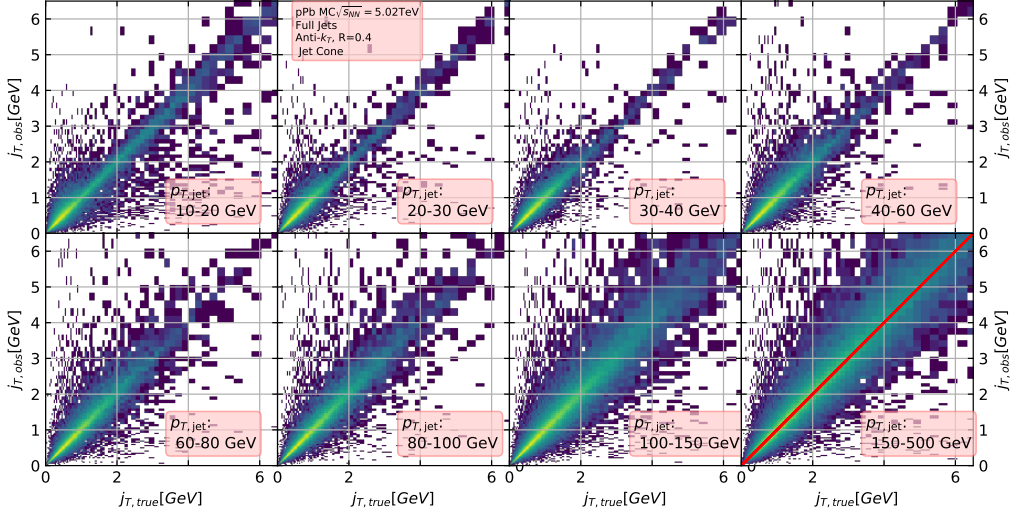


Figure 26: j_T Response matrices in single jet p_T bins

In the second method we randomly assign the tracks of event new ϕ and η values. The result is guaranteed to be uncorrelated.

6.4.1 Perpendicular cone background

After calculating the j_T values for tracks in the jet, we rotate the jet axis by $\frac{\pi}{2}$ in positive ϕ direction. We check that there are no other jets closer than $2R$ to the rotated axis. If there are then background calculation is skipped for this jet. Probability of this happening is 1-2% depending on the jet p_T bin.

If we don't find other jets in the vicinity we move on to estimate the background. We find all tracks within a cone of radius R around the rotated axis and calculate j_T of these tracks with respect to the rotated axis. Auto-correlations are added to match effect to jet. (see 6.4.3)

6.4.2 Random background

In the random background method we look at all tracks in the event, except for tracks close to jets found by the jet algorithm. We randomly assign new η and ϕ values to all tracks using uniform distribution. $|\eta| < 1.0$ p_T values are kept the same. To increase statistics there is a possibility to create a number of random tracks for each actual track. In the analysis we currently do this 10 times for each track. Again the track p_T value is kept the same.

We create a random jet cone from uniform η and ϕ distributions. Here $|\eta| < 0.25$. Now we calculate j_T of the random tracks with respect to the random cone

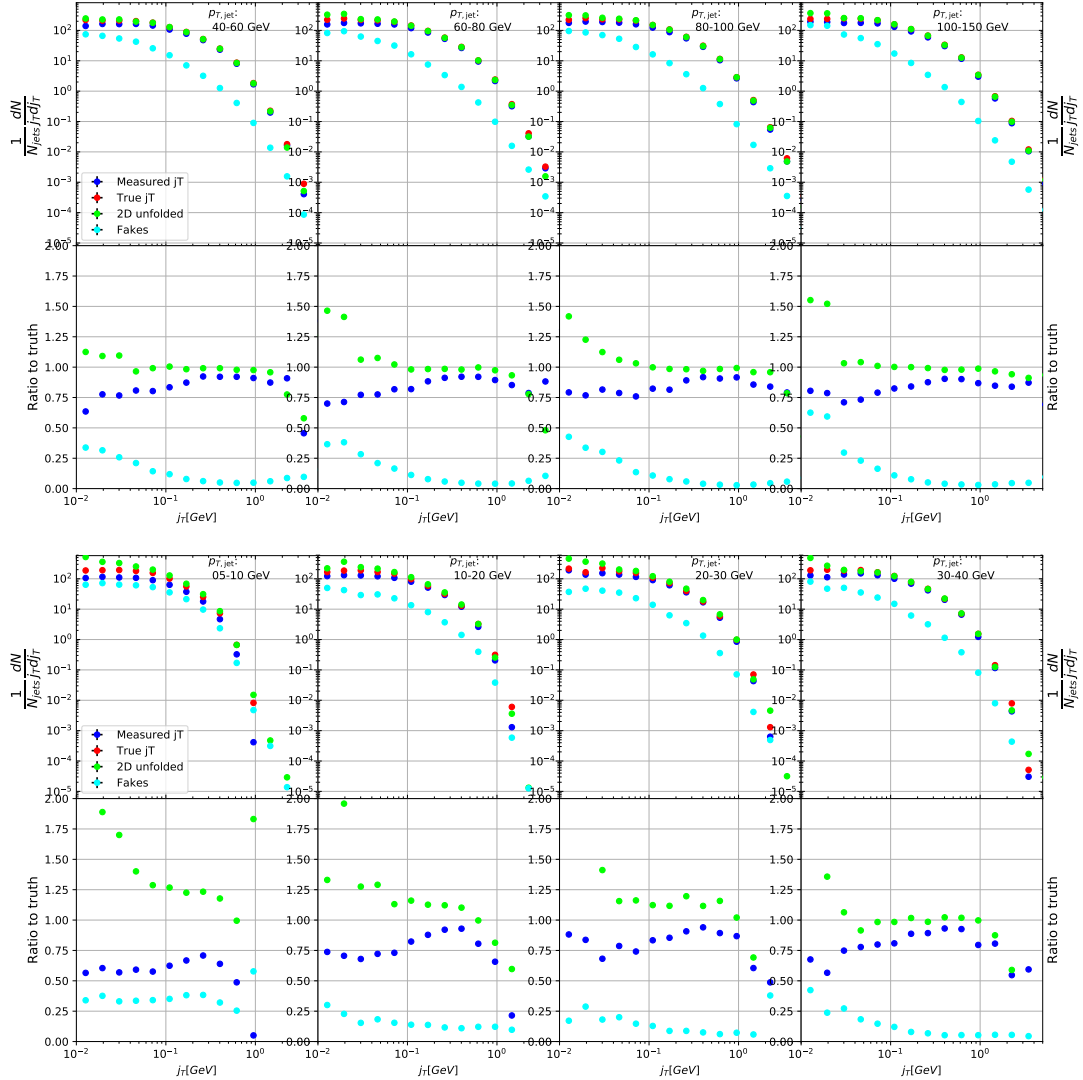
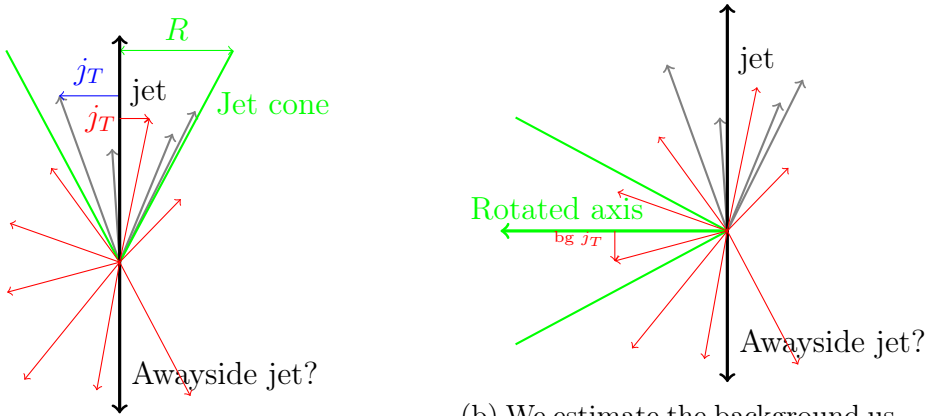
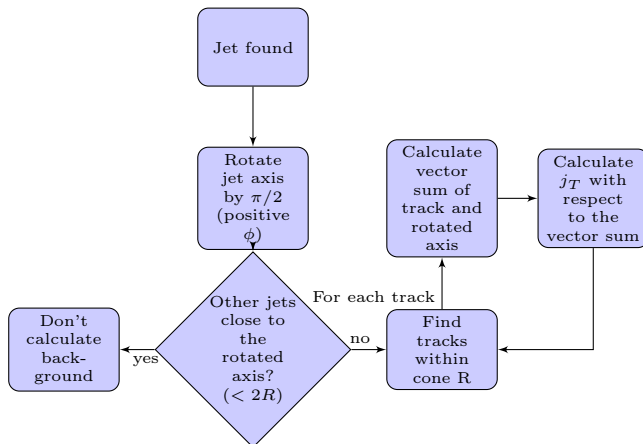


Figure 27: Pythia closure test results. Fake tracks include also tracks that do exist in the true dataset, but for one reason or another were not given j_T values. j_T is only calculated for tracks that are associated with jets



(a) Red is underlying event while gray tracks represent the signal
(b) We estimate the background using a cone where the axis is perpendicular to the jet axis



axis. Auto-correlations are added before calculating j_T (see 6.4.3)

6.4.3 Auto-correlations

Jet axis is simply a vector sum of all its constituents. Thus having an additional track in the jet from the underlying event moves the jet axis towards this track. Since the axis is now closer to the track, it has a smaller j_T value. Assuming a 1 GeV background track at the edge of a $R = 0.4$ the j_T value would be 0.4GeV. If this is added to a 5GeV jet, the j_T value becomes 0.33GeV. In a 50GeV jet it would be 0.39GeV. This is a region where the inclusive j_T distribution is dominated by background. The distribution is also steeply falling. Overestimating the background can lead to a situation where the background estimation exceeds the inclusive distribution.

To take this effect into account we can't use a fixed axis for background, but it has to behave like a jet would when additional tracks are added. Thus before calculating j_T values we make a vector sum of the track and the axis used for background, which is either the perpendicular cone axis or the random axis depending on the background method. In each case the momentum of this background axis is assumed to be the same as the jet which initiated the background estimation.

In pPb data there is on average about one underlying event track in a $R = 0.4$ cone.

Extend Background, Perp. cone vs. Random

6.5 Fitting

The resulting signal distribution are fitted with a 2 component function shown in Eq. 25. Gaussian distribution is used for low j_T and an inverse gamma function is used for high j_T . The gaussian is taken to have the center at $j_T = 0$. In total this gives 5 parameters.

$$\frac{1}{N_{\text{jets}} j_T \text{d}j_T} \frac{\text{d}N}{\text{d}j_T} = \frac{B_2}{B_1 \sqrt{2\pi}} e^{-\frac{j_T^2}{2B_1^2}} + \frac{B_3 B_5^{B_4}}{\Gamma(B_4)} \frac{e^{-\frac{B_5}{j_T}}}{j_T^{B_4+1}} \quad (25)$$

To achieve stable results the fitting is performed in two steps. First each component is fitted separately. Gaussian component is fitted to the low end in j_T . Inverse gamma component is fitted to j_T above 1 GeV/c. After getting the results from the individual fits they are combined into a single function with initial values from the individual results and an additional fit is performed. Fitting only the gaussian component to the entire distribution produces approximately the same result as the gaussian component in the two-component model.

After getting the fit function $\sqrt{\langle j_T^2 \rangle}$ (RMS) and yield values are extracted separately from each component. The narrow component RMS is

$$\sqrt{\langle j_T^2 \rangle} = \sqrt{2}B_1,$$

1265 and the wide component RMS value is calculated as

$$\sqrt{\langle j_T^2 \rangle} = \frac{B_5}{\sqrt{(B_4 - 2)(B_4 - 3)}},$$

1266 where it is required that $B_4 > 3$.

1267 7 Systematic uncertainties

1268 Extend Systematics

1269 The systematic uncertainties in this analysis come from the background esti-
1270 mation, the unfolding procedure and the cuts used to select the tracks. Tracking
1271 uncertainties are estimated from variations of the track selection cuts defined in
1272 Sec. 3. The resulting variations in RMS are shown in Table 4. The uncertainties
1273 from unfolding and background subtraction are of the same magnitude.

1274 The systematics in background estimation were studied using an alternative
1275 method to extract the background, mainly the random background method. The
1276 resulting uncertainty is below 5% for the wide component RMS and below 9% for
1277 the narrow component RMS.

1278 The systematic uncertainty that arises from the unfolding procedure is esti-
1279 mated by performing the unfolding with two separate methods. Data corrected
1280 by the iterative unfolding method are used as the results and the SVD unfolding
1281 method is employed to estimate the uncertainty. In a PYTHIA closure test the
1282 true distribution was in general found to be between the unfolded distributions
1283 from the iterative and SVD method. The difference between the methods when
1284 unfolding data should give a reasonable estimate of the unfolding uncertainty. The
1285 resulting uncertainty is below 8% for both wide and narrow component RMS.

1286 The different source of the systematic uncertainty are considered as uncorre-
1287 lated and the values of each source are summed in quadrature. The resulting
1288 uncertainty is 9 % for the wide component RMS and 12 % for the narrow compo-
1289 nent RMS.

1290 There is no tracking and no unfolding uncertainty in the Monte Carlo simula-
1291 tions.

Table 3: Summary of systematic errors

Systematic	Wide RMS	Narrow RMS
Background	5 %	9 %
Unfolding	8 %	8 %
Tracking	? %	? %
Total	9 %	12%

₁₂₉₂ 8 TPC Upgrade?

1293 9 Systematic errors

1294 9.1 Background subtraction

1295 Fits are performed on both perpendicular cone and random background signals.
 1296 Difference between them is taken as the systematic error. The fits for individ-
 1297 ual bins from the random background method are shown in figure 31. Resulting
 1298 differences between the methods for different components are shown in figure 30.

1299 9.2 Unfolding

1300 Unfolding is performed using both SVD and Bayesian unfolding. Difference be-
 1301 tween the methods is taken as the systematic error. Since SVD unfolding does
 1302 not have a 2 dimensional options, the unfolding is done bin by bin. The resulting
 1303 distributions after SVD unfolding and background subtraction with the perpendic-
 1304 ular cone method are shown in fig ???. Resulting differences between the methods
 1305 for different components are shown in figure 32.

1306 9.3 Tracking

1307 9.4 Combining systematics

1308 Resulting systematic errors are shown in table 4. Systematic errors are combined
 1309 bin-by-bin in quadrature to get the total systematic errors.

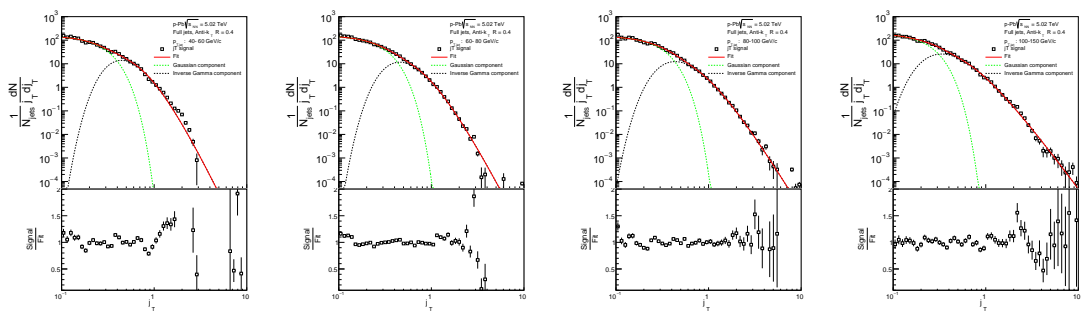


Figure 29: j_T signal with random background subtraction fits in different jet p_T bins

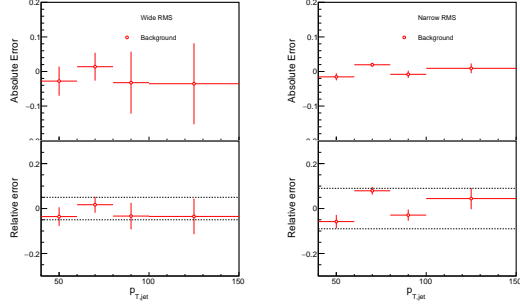


Figure 30: Differences between perpendicular cone and random background subtraction in the resulting RMS values.

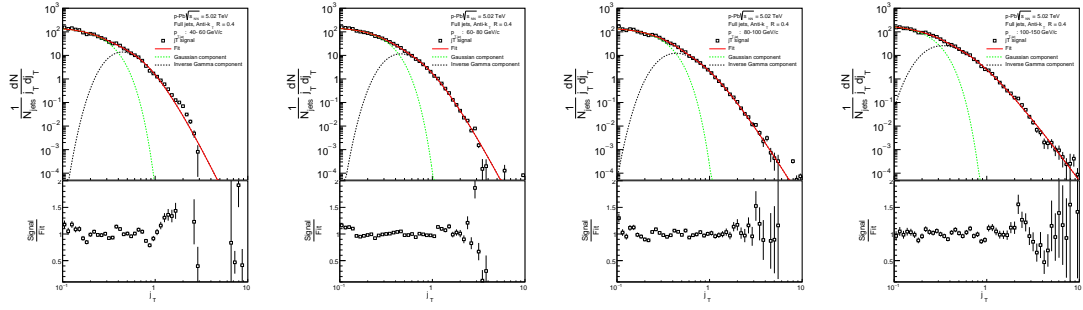


Figure 31: j_T signal with random background subtraction fits in different jet p_T bins

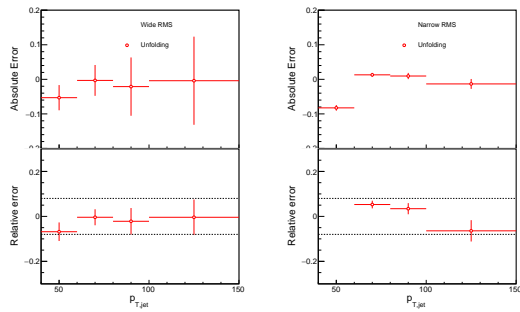


Figure 32: Differences between Bayesian and SVD unfolding in the resulting RMS values

Table 4: Summary of systematic errors

Systematic	Wide RMS	Narrow RMS
Background	5 %	9 %
Unfolding	8 %	8 %
Total	9 %	12%

1310 10 Results

1311 10.1 statistics

1312 Number of jets in different datasets and with different jet finders is shown in table
 1313 5. Background statistics for number of background cones (number of jets minus
 1314 number of discarded cones) are shown in table 6. Ratio of background cones to
 1315 number of jets is shown in table 7. The likelihood of having to discard a jet from
 background calculation is about 1-2%.

Table 5: Number of found jets by dataset and jet p_T bin

Jet p_T	5-10	10-20	20-30	30-40	40-60	60-80	80-100	100-150	150-500
MBFullR04	4969393	621753	32552	5584	1974	310	90	37	5
MBFullR05	4750567	826598	42373	5543	1719	276	73	29	3
MBChargedR04	3144538	673419	37783	4121	1009	148	36	12	1
MBChargedR05	2229247	175763	7961	1270	410	61	12	3	
TriggeredFullR04	187557	115927	78138	51317	39262	8621	2409	1167	171
TriggeredFullR05	99991	77147	48612	34325	28104	6342	1726	794	104
TriggeredChargedR04	37411	29945	18186	13148	11142	2517	675	326	44
TriggeredChargedR05	433155	175031	54789	19776	10626	1983	457	194	15

1316

Table 6: Number of background cones used in perpendicular cone background calculation

Jet p_T	5-10	10-20	20-30	30-40	40-60	60-80	80-100	100-150	150-500
MBFullR04	4947583	617895	32357	5548	1965	310	90	37	5
MBFullR05	4710217	815461	41584	5439	1698	273	73	29	3
MBChargedR04	3117495	661106	36739	4014	988	144	36	12	1
MBChargedR05	2195286	172919	7860	1249	406	61	12	3	
TriggeredFullR04	186574	115376	77949	51216	39196	8603	2405	1167	171
TriggeredFullR05	99102	76462	48320	34216	28038	6334	1722	794	103
TriggeredChargedR04	37160	29543	17988	13099	11129	2515	675	326	44
TriggeredChargedR05	313421	140707	45229	16243	8709	1604	377	154	14

Table 7: Ratio of background cone number to number of jets

MBFullR04	99.56%	99.38%	99.40%	99.36%	99.54%	100.00%	100.00%	100.00%	100.00%
MBFullR05	99.15%	98.65%	98.14%	98.12%	98.78%	98.91%	100.00%	100.00%	100.00%
MBChargedR04	99.14%	98.17%	97.24%	97.40%	97.92%	97.30%	100.00%	100.00%	100.00%
MBChargedR05	98.48%	98.38%	98.73%	98.35%	99.02%	100.00%	100.00%	100.00%	100.00%
TriggeredFullR04	99.48%	99.52%	99.76%	99.80%	99.83%	99.79%	99.83%	100.00%	100.00%
TriggeredFullR05	99.11%	99.11%	99.40%	99.68%	99.77%	99.87%	99.77%	100.00%	99.04%
TriggeredChargedR04	99.33%	98.66%	98.91%	99.63%	99.88%	99.92%	100.00%	100.00%	100.00%
TriggeredChargedR05	72.36%	80.39%	82.55%	82.13%	81.96%	80.89%	82.49%	79.38%	93.33%

1317 10.2 Data

1318 10.3 Background

1319 Comparison between perpendicular cone and random background in figure 33.

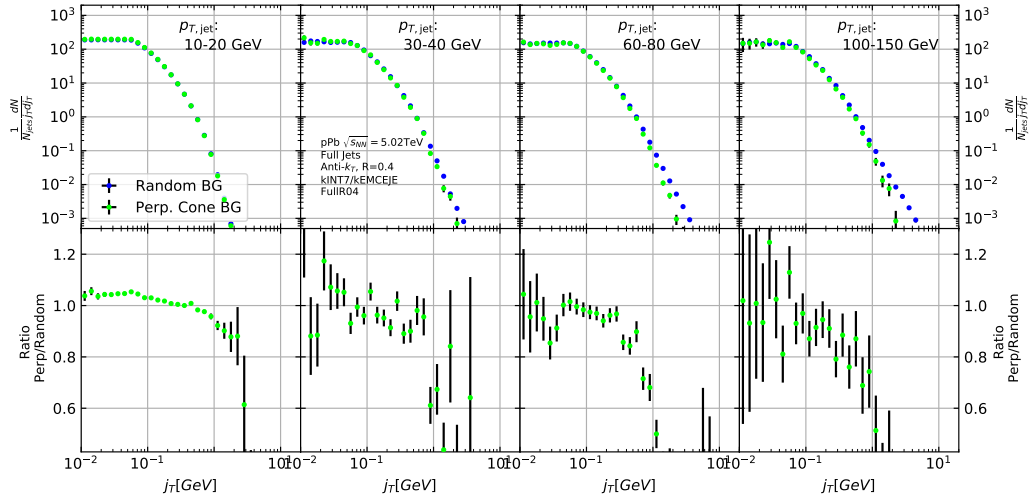


Figure 33: j_T background with two different methods

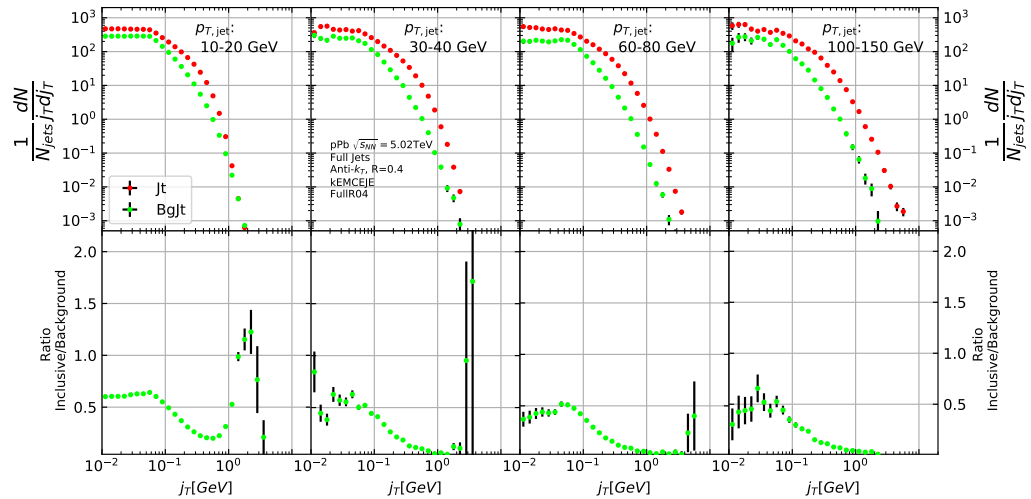


Figure 34: Inclusive j_T with background

1320 **10.4 Inclusive results**

1321 Results in figure 34

1322 **10.5 Comparison between A and C side**

1323 In 2013 there were some issues with tracking. To rule out effects on j_T distributions
1324 a study was performed comparing j_T distributions between A and C side. No
1325 systematic differences were observed.

1326 **10.6 Subtracted signal**

1327 Results in figure 36. Comparison between signals with different backgrounds in
1328 figure 37

1329 **10.7 Fitting**

1330 Fits of j_T distributions in different jet p_T bins with $p_T > 40\text{GeV}$ are shown in figure
1331 38. Additional jet p_T bins are shown in appendix ???. In lowest jet p_T bins the
1332 jets are mainly combinatorial which makes background subtraction and unfolding
1333 difficult and thus the signal can't be trusted.

1334 The fits describe the data well. There is some fluctuation of the order of 10 %
1335 around the fit function. At hight j_T the statistical errors in the signal are large.

1336 **10.7.1 Results**

1337 RMS and yield results with systematic errors are shown separately in figure 39.
1338 Figure 40 shows RMS values for both components combined. The figure also
1339 includes results from a PYTHIA simulation.

1340 **10.8 Comparison to dihadron results**

1341 Comparison to RMS values in dihadron analysis [?] are shown in figure Dihadron
1342 results from [?]. For comparison the dihadron trigger p_T bins are converted to jet
1343 p_T bins and vice versa. Bin-by-bin comparison is still not possible, but dihadron
1344 analysis gives systematically larger RMS values. This could be caused by several
1345 kinematical factors. In jet j_T analysis the jet cone limits possible j_T values and
1346 thus the width and RMS of the j_T distributions. The effect of this limitation can
1347 be studied by changing the cone size as is described in section 10.9.

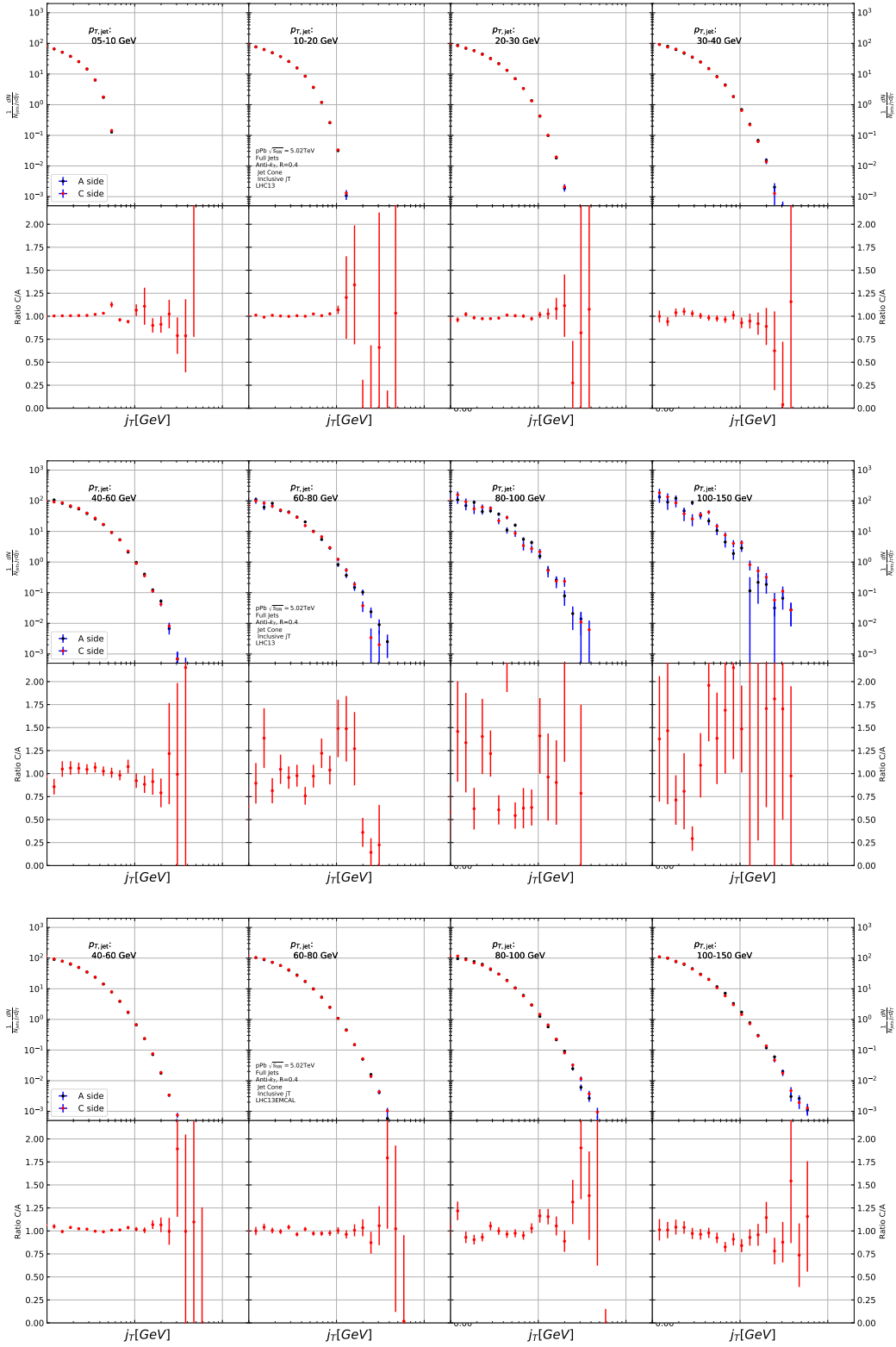


Figure 35: Comparison of inclusive j_T distributions between A and C side for minimum bias and EMCAL triggered data.

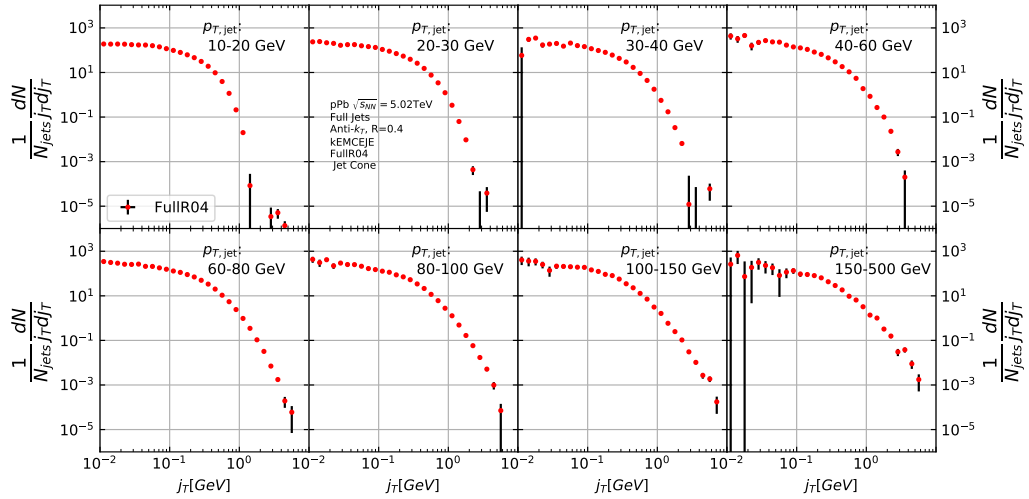


Figure 36: j_T signal with background subtracted

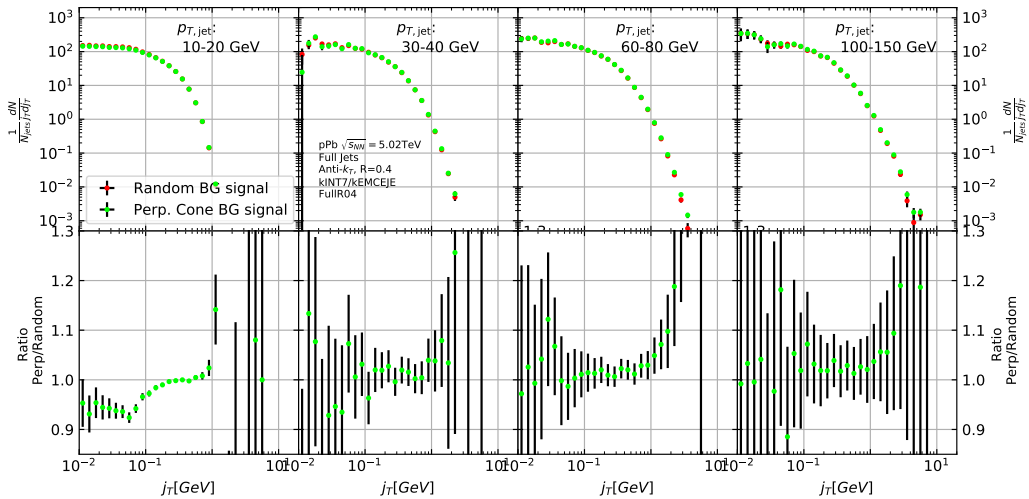


Figure 37: Comparison of the effect of background method on j_T signal.

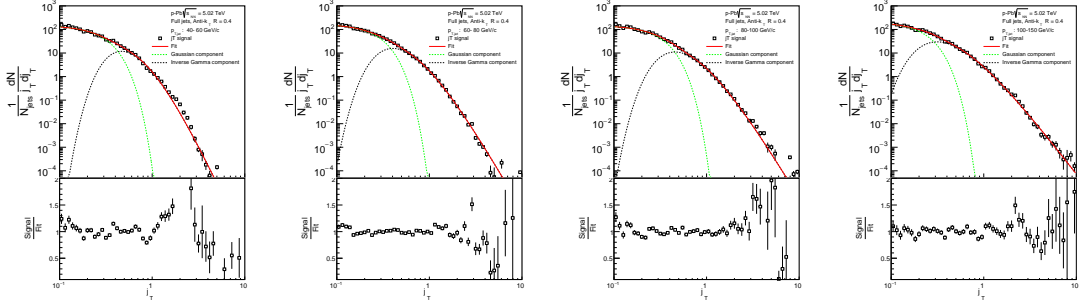


Figure 38: j_T signal fits in different jet p_T bins

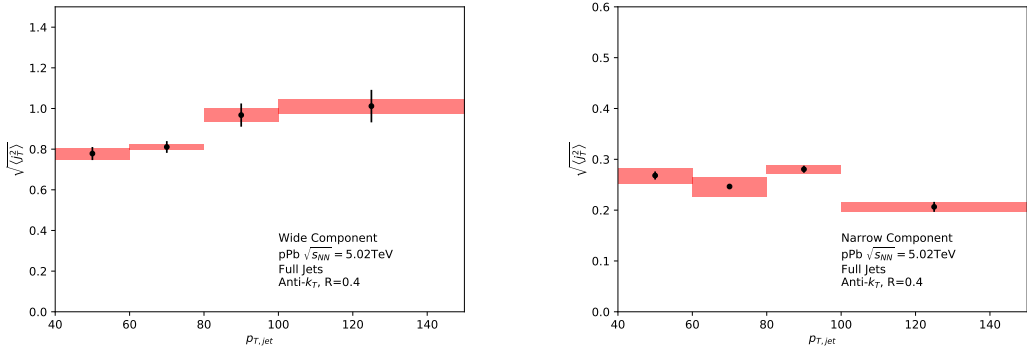


Figure 39: RMS values extracted from the fits for the gaussian (narrow) and inverse gamma (wide) components

1348 Comparison to j_T results from dihadron analysis [?] is shown in figure 44.
 1349 Trigger p_T bins used in dihadron analysis are converted to jet p_T bins using ob-
 1350 served average jet p_T values in leading track momentum bins. Similarly jet p_T bins
 1351 are converted to $p_{T,\text{trigger}}$ bins using average leading track p_T values in $p_{T,\text{jet}}$ bins.

1352 The trends are similar in dihadron and jet j_T results. Wide component RMS
 1353 values tend to increase with increasing $p_{T,\text{trigger}}/p_{T,\text{jet}}$. Narrow component RMS
 1354 increases slightly in dihadron analysis but not in jet j_T , WHY? (Depends on x_{\parallel}
 1355 bin in dihadron)

1356 In general dihadron j_T gives wider distributions with larger RMS values. In
 1357 jet analysis the cone size limits width and thus the RMS values. The effect of this
 1358 limitation can be studied by changing the cone size as is described in section 10.9.

1359 Additionally the leading track is an imperfect estimate of the jet/original par-
 1360 ton. Because the leading track in general is at an angle compared to the jet axis,
 1361 the resulting j_T values are different. In practice the jet axis found by the jet finding
 1362 algorithm tends to minimize the average j_T of jet constituents. Thus the yield at

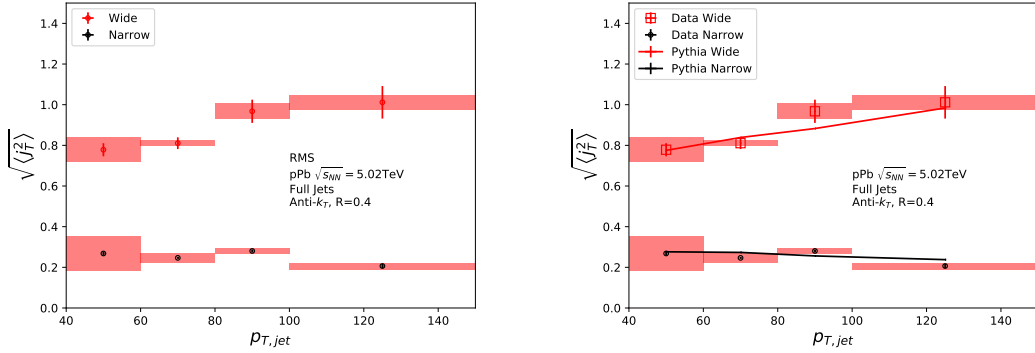


Figure 40: RMS values extracted from the fits for the gaussian (narrow) and inverse gamma (wide) components

¹³⁶³ high j_T is limited and the RMS values are smaller.

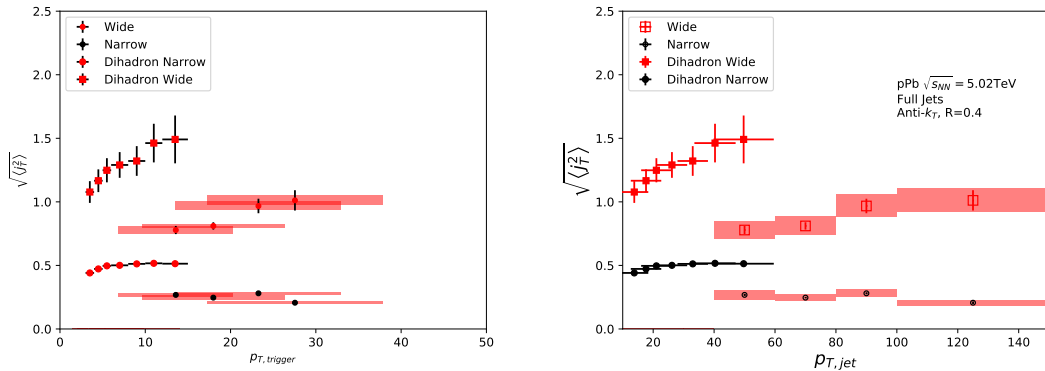


Figure 41: Jet j_T results are compared to results obtained in the dihadron analysis. This is done both in jet p_T and trigger p_T bins by converting between them.

¹³⁶⁴ 10.9 Different R parameters

¹³⁶⁵ Study the effect of cone sizes on j_T distribution in particle level Pythia.

¹³⁶⁶ Increasing the cone size of jets gives more room for high j_T tracks. This is seen
¹³⁶⁷ in the individual j_T distributions as increased high j_T production. At low j_T there
¹³⁶⁸ is no change.

¹³⁶⁹ When looking at RMS values from wide component we see an increase/decrease
¹³⁷⁰ of about 10% when going from $R = 0.4$ to $R = 0.5/R = 0.3$.

1371 The message from narrow component RMS values is less clear. At low jet p_T
 the behaviour is similar, but at high p_T the order is reversed.

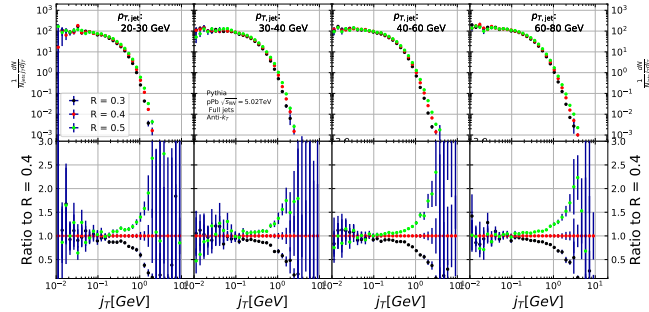


Figure 42: Effect of changing R parameter in jet finding on j_T distributions

1372

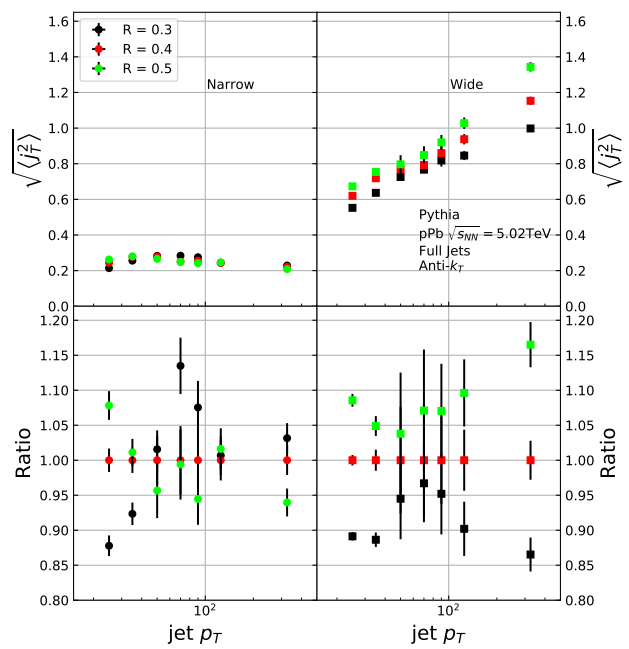


Figure 43: Effect of changing R parameter in jet finding on narrow and wide component RMS values. Wide component RMS values increase with increasing cone size.

1373 11 Discussion

1374 11.1 Discussion

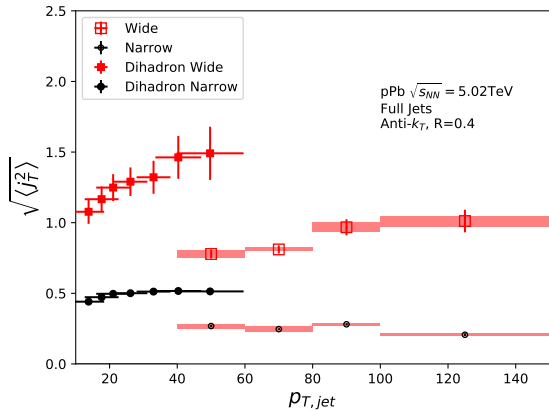


Figure 44: Comparison of results with dihadron j_T results. Dihadron trigger p_T bins are converted to jet p_T bins using observed mean $p_{T,jet}$ values in $p_{T,trigger}$ bins. Dihadron results are for $0.2 < x_{||} < 0.4$

1375 Comparison to j_T results from dihadron analysis [107] is shown in Fig. 44.
 1376 Trigger p_T bins used in dihadron analysis are converted to jet p_T bins using ob-
 1377 served average jet p_T values in leading track momentum bins. Similarly jet p_T bins
 1378 are converted to $p_{T,trigger}$ bins using average leading track p_T values in $p_{T,jet}$ bins.

1379 The trends are similar in dihadron and jet j_T results. Wide component RMS
 1380 values tend to increase with increasing $p_{T,trigger}/p_{T,jet}$. Narrow component RMS
 1381 increases slightly in dihadron analysis but not in jet j_T , WHY? (Depends on $x_{||}$
 1382 bin in dihadron)

1383 In general dihadron j_T gives wider distributions with larger RMS values. In
 1384 jet analysis the cone size limits width and thus the RMS values. With increasing
 1385 cone size one gets increasing wide RMS values as seen in Fig. 45. This should be
 1386 the dominant factor.

1387 Effect of the R parameter choice is studied in PYTHIA. Having a fixed cone
 1388 puts hard limits on the possible j_T values. Increasing the cone size loosens these
 1389 limits and allows higher j_T values. The results are shown in Fig. 45. Left hand
 1390 side shows the j_T distributions. There is very little change in low j_T but at high
 1391 j_T the yield increases.

1392 This is also seen in the RMS values shown in the right hand side of Fig. 45,
 1393 where the change in wide component RMS is about 10% when going from $R = 0.4$
 1394 to $R = 0.3$ or $R = 0.5$. With the narrow component values the situation is less



Figure 45: Effect of changing R parameter in jet finding on j_T distributions

clear. At low jet p_T larger R parameter leads to larger RMS values, but at high $p_{T\text{jet}}$ the situation is reversed; increasing the R parameter decreases RMS values.

Additionally the leading track is an imperfect estimate of the jet/original parton. Because the leading track in general is at an angle compared to the jet axis, the resulting j_T values are different. In practice the jet axis found by the jet finding algorithm tends to minimize the average j_T of jet constituents. Thus the yield at high j_T is limited and the RMS values are smaller.

A PYTHIA study was performed where j_T was calculated with respect to the leading track momentum, instead of the jet axis. The results are shown in Fig. 46. The resulting j_T distributions are significantly wider than j_T distributions from the typical method. The effect seems to be larger than the effect seen in comparing different R values.

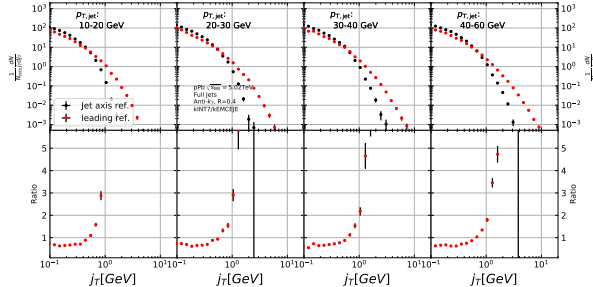


Figure 46: Results of calculating j_T with respect to the jet axis or the leading hadron. The assumption is that because the leading hadron is an imperfect estimate of the jet axis, low j_T tracks should on average be shifted to higher j_T

1407 12 Summary

1408 In this work two distinct j_T components were extracted for narrow and wide contri-
1409 butions using jet reconstruction. RMS values for both components were obtained.
1410 The width of the wide component is found to increase for increasing $p_{T\text{jet}}$. This
1411 is in part explained by the changing kinematical limits when going to higher $p_{T\text{jet}}$
1412 which allows higher $p_{T\text{track}}$. Additionally the larger phase space allows stronger
1413 parton splitting. The results are qualitatively compatible with previous studies
1414 that studied j_T using two-particle correlations.

₁₄₁₅ **References**

- ₁₄₁₆ [1] PHENIX Collaboration, K. Adcox *et al.*, Nucl.Phys. **A757**, 184 (2005), nucl-ex/0410003.
- ₁₄₁₇ [2] STAR Collaboration, J. Adams *et al.*, Nucl.Phys. **A757**, 102 (2005), nucl-ex/0501009.
- ₁₄₁₈ [3] J.-Y. Ollitrault, Phys. Rev. D **46**, 229 (1992).
- ₁₄₁₉ [4] U. Heinz and P. Kolb, Nucl. Phys. **A702**, 269 (2002).
- ₁₄₂₀ [5] E. Shuryak, Prog. Part. Nucl. Phys. **62**, 48 (2009).
- ₁₄₂₁ [6] ATLAS Collaboration, J. Jia, Nucl.Phys.A904-905 **2013**, 421c (2013), 1209.4232.
- ₁₄₂₂ [7] R. A. Lacey *et al.*, (2012), 1207.1886.
- ₁₄₂₃ [8] R. Bjorklund, W. Crandall, B. J. Moyer, and H. York, Phys. Review **77**, 213 (1950).
- ₁₄₂₄ [9] W. Heisenberg, Zeitschrift für Physik **77**, 1 (1932).
- ₁₄₂₅ [10] M. Gell-Mann, Phys. Rev. **125**, 1067 (1962).
- ₁₄₂₆ [11] M. Gell-Mann, Phys. Lett. **8**, 214 (1964).
- ₁₄₂₇ [12] O. Greenberg, Phys. Rev. Lett. **13**, 598 (1964).
- ₁₄₂₈ [13] Crystal Ball Collaboration, D. Williams *et al.*, Phys.Rev. **D38**, 1365 (1988).
- ₁₄₂₉ [14] W. Krolikowski, Nuovo Cim. **A27**, 194 (1975).
- ₁₄₃₀ [15] D. J. Gross and F. Wilczek, Physical Review Letters **30**, 1343 (1973).
- ₁₄₃₁ [16] H. D. Politzer, Physical Review Letters **30**, 1346 (1973).
- ₁₄₃₂ [17] D. J. Gross and F. Wilczek, Physical Review D **8**, 3633 (1973).
- ₁₄₃₃ [18] D. J. Gross and F. Wilczek, Physical Review D **9**, 980 (1974).
- ₁₄₃₄ [19] H. Georgi and H. D. Politzer, Physical Review D **9**, 416 (1974).
- ₁₄₃₅ [20] H. Fritzsch, M. Gell-Mann, and H. Leutwyler, Physics Letters B **47**, 365 (1973).
- ₁₄₃₆ [21] H. Fritzsch, M. Gell-Mann, and H. Leutwyler, Physics Letters B **47**, 365 (1973).
- ₁₄₃₇ [22] H. Fritzsch, M. Gell-Mann, and H. Leutwyler, Physics Letters B **47**, 365 (1973).
- ₁₄₃₈ [23] H. Fritzsch, M. Gell-Mann, and H. Leutwyler, Physics Letters B **47**, 365 (1973).
- ₁₄₃₉ [24] H. Fritzsch, M. Gell-Mann, and H. Leutwyler, Physics Letters B **47**, 365 (1973).
- ₁₄₄₀ [25] H. Fritzsch, M. Gell-Mann, and H. Leutwyler, Physics Letters B **47**, 365 (1973).

- ¹⁴⁴¹ [21] I. Flegel and P. Söding, CERN courier (2004).
- ¹⁴⁴² [22] R. Brandelik *et al.*, Physics Letters B **86**, 243 (1979).
- ¹⁴⁴³ [23] J. K. L. MacDonald, Phys. Rev. **43**, 830 (1933).
- ¹⁴⁴⁴ [24] C. Berger *et al.*, Physics Letters B **86**, 418 (1979).
- ¹⁴⁴⁵ [25] J. Collins and M. Perry, Phys. rev. Lett. **34**, 1353 (1975).
- ¹⁴⁴⁶ [26] E. Shuryak, Phys. Reps. **61**, 71 (1980).
- ¹⁴⁴⁷ [27] K. Rajagopal, SLAC Beam Line **31-2**, 9 (2001).
- ¹⁴⁴⁸ [28] P. Kovtun, D. Son, and A. Starinets, Phys.Rev.Lett. **94**, 111601 (2005), hep-th/0405231.
- ¹⁴⁵⁰ [29] R. A. Lacey *et al.*, Phys. Rev. Lett. **98**, 092301 (2007).
- ¹⁴⁵¹ [30] E. Lofgren, *ACCELERATOR DIVISION ANNUAL REPORTS, 1 JULY 1972 12/31/1974* (, 1975).
- ¹⁴⁵³ [31] D. S. Barton, Heavy ion program at bnl: Ags, rhic, in *Proc. 1987 Particle Accelerator Conference, Washington, D.C., March, 1987*.
- ¹⁴⁵⁵ [32] I. Vitev and M. Gyulassy, Phys.Rev.Lett. **89**, 252301 (2002), hep-ph/0209161.
- ¹⁴⁵⁷ [33] S. Choi and K. S. Lee, Phys. Rev. C **84**, 064905 (2011).
- ¹⁴⁵⁸ [34] A. Kovalenko *et al.*, Status of the nuclotron, in *Proceedings of EPAC Vol. 94*, pp. 161–164, 1994.
- ¹⁴⁶⁰ [35] NA61/SHINE, K. Grebieszkow, PoS **CPOD2013**, 004 (2013).
- ¹⁴⁶¹ [36] BRAHMS Collaboration, I. Arsene *et al.*, Nucl.Phys. **A757**, 1 (2005), nucl-ex/0410020.
- ¹⁴⁶³ [37] B. Back *et al.*, Nucl.Phys. **A757**, 28 (2005), nucl-ex/0410022.
- ¹⁴⁶⁴ [38] S. A. Voloshin, A. M. Poskanzer, and R. Snellings, (2008), 0809.2949.
- ¹⁴⁶⁵ [39] S. A. Voloshin, A. M. Poskanzer, A. Tang, and G. Wang, Phys.Lett. **B659**, 537 (2008), 0708.0800.
- ¹⁴⁶⁷ [40] H. Holopainen, H. Niemi, and K. J. Eskola, Phys.Rev. **C83**, 034901 (2011), 1007.0368.

- ¹⁴⁶⁹ [41] ALICE Collaboration, Phys. Rev. C **88**, 044909 (2013).
- ¹⁴⁷⁰ [42] M. L. Miller, K. Reygers, S. J. Sanders, and P. Steinberg,
¹⁴⁷¹ Ann.Rev.Nucl.Part.Sci. **57**, 205 (2007), nucl-ex/0701025.
- ¹⁴⁷² [43] R. Glauber, Lectures in theoretical physics, 1959.
- ¹⁴⁷³ [44] W. Czyż and L. Maximon, Annals of Physics **52**, 59 (1969).
- ¹⁴⁷⁴ [45] A. Białłas, M. Bleszyński, and W. Czyż, Nuclear Physics B **111**, 461 (1976).
- ¹⁴⁷⁵ [46] PHENIX Collaboration, S. Afanasiev *et al.*, Phys.Rev. **C80**, 054907 (2009),
¹⁴⁷⁶ 0903.4886.
- ¹⁴⁷⁷ [47] J.-Y. Ollitrault, Eur.J.Phys. **29**, 275 (2008), 0708.2433.
- ¹⁴⁷⁸ [48] P. Romatschke, Int.J.Mod.Phys. **E19**, 1 (2010), 0902.3663.
- ¹⁴⁷⁹ [49] L. LD, Izv. Akad. Nauk Ser. Fiz. **17**, 51 (1953).
- ¹⁴⁸⁰ [50] H. Song, S. Bass, and U. W. Heinz, (2013), 1311.0157.
- ¹⁴⁸¹ [51] H. Niemi, G. Denicol, P. Huovinen, E. Molnar, and D. Rischke, Phys.Rev.
¹⁴⁸² **C86**, 014909 (2012), 1203.2452.
- ¹⁴⁸³ [52] K. A. *et al.* [ALICE Collaboration], Phys. Rev. Lett **106** (2011), 032301.
- ¹⁴⁸⁴ [53] J.-Y. Ollitrault, Phys.Rev. D **48**, 1132 (1993), hep-ph/9303247.
- ¹⁴⁸⁵ [54] P. Danielewicz and G. Odyniec, Physics Letters B **157**, 146 (1985).
- ¹⁴⁸⁶ [55] P. Danielewicz and M. Gyulassy, Physics Letters B **129**, 283 (1983).
- ¹⁴⁸⁷ [56] T. Abbott *et al.*, Phys. Rev. Lett. **70**, 1393 (1993).
- ¹⁴⁸⁸ [57] S. Voloshin and Y. Zhang, Z.Phys. **C70**, 665 (1996), hep-ph/9407282.
- ¹⁴⁸⁹ [58] E877 Collaboration, J. Barrette *et al.*, Phys.Rev.Lett. **73**, 2532 (1994), hep-
¹⁴⁹⁰ ex/9405003.
- ¹⁴⁹¹ [59] CMS Collaboration, S. Chatrchyan *et al.*, Phys.Rev.Lett. **109**, 022301
¹⁴⁹² (2012), 1204.1850.
- ¹⁴⁹³ [60] A. Majumder and M. Van Leeuwen, Prog.Part.Nucl.Phys. **A66**, 41 (2011),
¹⁴⁹⁴ 1002.2206.

- 1495 [61] F. Dominguez, C. Marquet, A. Mueller, B. Wu, and B.-W. Xiao, Nucl.Phys.
1496 **A811**, 197 (2008), 0803.3234.
- 1497 [62] M. Gyulassy, P. Levai, and I. Vitev, Nucl.Phys. **B571**, 197 (2000), hep-ph/9907461.
- 1499 [63] U. A. Wiedemann, Nucl.Phys. **B588**, 303 (2000), hep-ph/0005129.
- 1500 [64] P. B. Arnold, G. D. Moore, and L. G. Yaffe, JHEP **0112**, 009 (2001), hep-ph/0111107.
- 1502 [65] X.-N. Wang and X.-f. Guo, Nucl.Phys. **A696**, 788 (2001), hep-ph/0102230.
- 1503 [66] T. Sjostrand, S. Mrenna, and P. Z. Skands, Comput.Phys.Commun. **178**,
1504 852 (2008), 0710.3820.
- 1505 [67] I. Lokhtin and A. Snigirev, Eur.Phys.J. **C45**, 211 (2006), hep-ph/0506189.
- 1506 [68] N. Armesto, L. Cunqueiro, and C. A. Salgado, Nucl.Phys. **A830**, 271C
1507 (2009), 0907.4706.
- 1508 [69] K. Zapp, G. Ingelman, J. Rathsman, J. Stachel, and U. A. Wiedemann,
1509 Eur.Phys.J. **C60**, 617 (2009), 0804.3568.
- 1510 [70] T. Renk, Phys.Rev. **C79**, 054906 (2009), 0901.2818.
- 1511 [71] ALICE Collaboration, K. Aamodt *et al.*, Phys.Lett. **B696**, 30 (2011),
1512 1012.1004.
- 1513 [72] WA98 Collaboration, M. Aggarwal *et al.*, Eur.Phys.J. **C23**, 225 (2002),
1514 nucl-ex/0108006.
- 1515 [73] D. G. d'Enterria, Phys.Lett. **B596**, 32 (2004), nucl-ex/0403055.
- 1516 [74] PHENIX Collaboration, A. Adare *et al.*, Phys.Rev.Lett. **101**, 232301 (2008),
1517 0801.4020.
- 1518 [75] STAR Collaboration, J. Adams *et al.*, Phys.Rev.Lett. **91**, 172302 (2003),
1519 nucl-ex/0305015.
- 1520 [76] A. Dainese, C. Loizides, and G. Paic, Eur.Phys.J. **C38**, 461 (2005), hep-ph/0406201.
- 1522 [77] I. Vitev, J.Phys. **G30**, S791 (2004), hep-ph/0403089.
- 1523 [78] C. A. Salgado and U. A. Wiedemann, Phys.Rev. **D68**, 014008 (2003), hep-ph/0302184.

- ₁₅₂₅ [79] N. Armesto, A. Dainese, C. A. Salgado, and U. A. Wiedemann, Phys.Rev. **D71**, 054027 (2005), hep-ph/0501225.
- ₁₅₂₇ [80] T. Renk, H. Holopainen, R. Paatelainen, and K. J. Eskola, Phys.Rev. **C84**, 014906 (2011), 1103.5308.
- ₁₅₂₉ [81] CMS Collaboration, S. Chatrchyan *et al.*, Eur.Phys.J. **C72**, 1945 (2012), 1202.2554.
- ₁₅₃₁ [82] PHENIX Collaboration, S. Afanasiev *et al.*, Phys. Rev. C **80**, 054907 (2009).
- ₁₅₃₂ [83] ALICE Collaboration, K. Aamodt *et al.*, Phys.Rev.Lett. **108**, 092301 (2012), 1110.0121.
- ₁₅₃₄ [84] J. L. Nagle and W. A. Zajc, Ann. Rev. Nucl. Part. Sci. **68**, 211 (2018), 1801.03477.
- ₁₅₃₆ [85] E735, T. Alexopoulos *et al.*, Phys. Rev. **D48**, 984 (1993).
- ₁₅₃₇ [86] MiniMax, T. C. Brooks *et al.*, Phys. Rev. **D61**, 032003 (2000), hep-ex/9906026.
- ₁₅₃₉ [87] C. Shen, Z. Qiu, and U. Heinz, Phys. Rev. **C92**, 014901 (2015), 1502.04636.
- ₁₅₄₀ [88] PHENIX, A. Adare *et al.*, Phys. Rev. **C94**, 064901 (2016), 1509.07758.
- ₁₅₄₁ [89] C. A. Salgado and J. P. Wessels, Ann. Rev. Nucl. Part. Sci. **66**, 449 (2016).
- ₁₅₄₂ [90] M. Gyulassy, I. Vitev, X.-N. Wang, and B.-W. Zhang, p. 123 (2003), nucl-th/0302077.
- ₁₅₄₄ [91] E. Norbeck, K. Šafařík, and P. A. Steinberg, Annual Review of Nuclear and Particle Science **64**, 383 (2014), <https://doi.org/10.1146/annurev-nucl-102912-144532>.
- ₁₅₄₇ [92] A. Accardi, F. Arleo, W. K. Brooks, D. D'Enterria, and V. Muccifora, Riv. Nuovo Cim. **32**, 439 (2010), 0907.3534.
- ₁₅₄₉ [93] ALICE, K. Aamodt *et al.*, JINST **3**, S08002 (2008).
- ₁₅₅₀ [94] ALICE, B. B. Abelev *et al.*, Int. J. Mod. Phys. **A29**, 1430044 (2014), 1402.4476.
- ₁₅₅₂ [95] ALICE, K. Aamodt *et al.*, JINST **5**, P03003 (2010), 1001.0502.
- ₁₅₅₃ [96] J. Alme *et al.*, Nucl. Instrum. Meth. **A622**, 316 (2010), 1001.1950.

- ₁₅₅₄ [97] ALICE, B. Abelev *et al.*, JHEP **03**, 053 (2012), 1201.2423.
- ₁₅₅₅ [98] ALICE, P. Cortese *et al.*, (2008).
- ₁₅₅₆ [99] J. Allen *et al.*, Report No. CERN-LHCC-2010-011. ALICE-TDR-14-add-1,
₁₅₅₇ 2010 (unpublished).
- ₁₅₅₈ [100] ALICE, G. Dellacasa *et al.*, (1999).
- ₁₅₅₉ [101] ALICE Collaboration, *Technical Design Report on Forward Detectors: FMD, T0 and V0*, 2004.
- ₁₅₆₁ [102] ALICE, B. Abelev *et al.*, Phys. Lett. **B719**, 29 (2013), 1212.2001.
- ₁₅₆₂ [103] M. Cacciari, G. P. Salam, and G. Soyez, Eur. Phys. J. **C72**, 1896 (2012),
₁₅₆₃ 1111.6097.
- ₁₅₆₄ [104] M. Cacciari, G. P. Salam, and G. Soyez, JHEP **04**, 063 (2008), 0802.1189.
- ₁₅₆₅ [105] T. Sjöstrand, S. Mrenna, and P. Z. Skands, Comput. Phys. Commun. **178**,
₁₅₆₆ 852 (2008), 0710.3820.
- ₁₅₆₇ [106] Roounfold: Root unfolding framework, <http://hepunx.rl.ac.uk/~adye/software/unfold/RooUnfold.html>, 2013.
- ₁₅₆₉ [107] <https://alice-publications.web.cern.ch/node/3655>, 2018.